Monthly Notices
of the
ROYAL ASTRONOMICAL SOCIETY

MNRAS **430,** 2513–2533 (2013) doi:10.1093/mnras/sts612

SCUBA-2: the 10 000 pixel bolometer camera on the James Clerk Maxwell Telescope

W. S. Holland,[1,2]★ D. Bintley,[3] E. L. Chapin,[3,4]† A. Chrysostomou,[3]‡ G. R. Davis,[3] J. T. Dempsey,[3] W. D. Duncan,[1,5]§ M. Fich,[6] P. Friberg,[3] M. Halpern,[4] K. D. Irwin,[5] T. Jenness,[3] B. D. Kelly,[1] M. J. MacIntosh,[1] E. I. Robson,[1] D. Scott,[4] P. A. R. Ade,[7] E. Atad-Ettedgui,[1] D. S. Berry,[3] S. C. Craig,[3]¶ X. Gao,[1] A. G. Gibb,[4] G. C. Hilton,[5] M. I. Hollister,[2]|| J. B. Kycia,[6] D. W. Lunney,[1] H. McGregor,[1]★★ D. Montgomery,[1] W. Parkes,[8] R. P. J. Tilanus,[3] J. N. Ullom,[5] C. A. Walther,[3] A. J. Walton,[8] A. L. Woodcraft,[7]†† M. Amiri,[4] D. Atkinson,[1] B. Burger,[4] T. Chuter,[3] I. M. Coulson,[3] W. B. Doriese,[5] C. Dunare,[8] F. Economou,[3]‡‡ M. D. Niemack,[5] H. A. L. Parsons,[3] C. D. Reintsema,[5] B. Sibthorpe,[1] I. Smail,[9] R. Sudiwala[7] and H. S. Thomas[3]

[1] *UK Astronomy Technology Centre, Royal Observatory, Blackford Hill, Edinburgh EH9 3HJ, UK*
[2] *Institute for Astronomy, Royal Observatory, University of Edinburgh, Blackford Hill, Edinburgh EH9 3HJ, UK*
[3] *Joint Astronomy Centre, 660 N. A'ohōkū Place, University Park, Hilo, HI 96720, USA*
[4] *Department of Physics & Astronomy, University of British Columbia, 6224 Agricultural Road, Vancouver, BC V6T 1Z1, Canada*
[5] *National Institute of Standards and Technology, 325 Broadway, Boulder, CO 80305, USA*
[6] *Department of Physics, University of Waterloo, Waterloo, ON N2L 3G1, Canada*
[7] *School of Physics & Astronomy, Cardiff University, 5 The Parade, Cardiff CF24 3AA, UK*
[8] *Scottish Microelectronics Centre, University of Edinburgh, West Mains Road, Edinburgh EH9 3JF, UK*
[9] *Institute for Computational Cosmology, Durham University, South Road, Durham DH1 3LE, UK*

Accepted 2012 December 12. Received 2012 December 11; in original form 2012 September 14

ABSTRACT

Submillimetre Common-User Bolometer Array 2 (SCUBA-2) is an innovative 10 000 pixel bolometer camera operating at submillimetre wavelengths on the James Clerk Maxwell Telescope (JCMT). The camera has the capability to carry out wide-field surveys to unprecedented depths, addressing key questions relating to the origins of galaxies, stars and planets. With two imaging arrays working simultaneously in the atmospheric windows at 450 and 850 μm, the vast increase in pixel count means that SCUBA-2 maps the sky 100–150 times faster than the previous SCUBA instrument. In this paper, we present an overview of the instrument, discuss the physical characteristics of the superconducting detector arrays, outline the observing modes and data acquisition, and present the early performance figures on the telescope. We also showcase the capabilities of the instrument via some early examples of the science SCUBA-2 that have already been undertaken. In 2012 February, SCUBA-2 began a series of unique legacy surveys for the JCMT community. These surveys will take 2.5 yr and the results are already providing complementary data to the shorter wavelength, shallower, larger area surveys

★ E-mail: wayne.holland@stfc.ac.uk
† Present address: XMM SOC, ESAC, Apartado 79, 28691 Villaneueva de la Canada, Madrid, Spain.
‡ Present address: School of Physics, Astronomy and Mathematics, University of Hertfordshire, Hatfield, Hertfordshire AL10 9AB, UK.
§ Present address: Intellectual Ventures, 3150 139th Ave SE, Building 4, Bellevue, WA 98005, USA.
¶ Present address: National Solar Observatory, Advanced Technology Solar Telescope, 950 N. Cherry Avenue, Tucson, AZ 85719, USA.
|| Present address: California Institute of Technology, 1200 East California Boulevard, Pasadena, CA 91125, USA.
★★ Present address: Institute for Astronomy, 2680 Woodlawn Drive, Honolulu, HI 96822, USA.
†† Present address: QMC Instruments, School of Physics, and Astronomy, Cardiff University, 5 The Parade, Cardiff CF24 3AA, UK.
‡‡ Present address: National Optical Astronomy Observatory, 950 N. Cherry Avenue, Tucson, AZ 85719, USA.

from *Herschel*. The SCUBA-2 surveys will also provide a wealth of information for further study with new facilities such as ALMA, and future telescopes such as CCAT and *SPICA*.

Key words: instrumentation: detectors – submillimetre: general.

1 INTRODUCTION

The submillimetre waveband, which encompasses the spectral range from 0.3 to 1 mm, contains a wealth of information about the cold Universe. Observations of gas and dust probe the earliest stages in the formation of galaxies, stars and planets. For example, the blackbody emission of a 10 K source (or a 40 K source at redshift $\sim$3) will peak around 300 μm. The continuum emission from dust is usually optically thin, so observations can probe to the heart of the most crucial processes, with the consequence that, for example, embryonic star-forming core masses and the surrounding structure of their molecular clouds are determined in a less model-dependent way than in the optical and infrared (IR) (e.g. Di Francesco et al. 2007; Ward-Thompson et al. 2007). On larger scales, much of the ultraviolet/optical light emitted from stars inside young galaxies is trapped within enshrouding dust clouds and re-emitted in the submillimetre. Only by observing at these longer wavelengths can the total energy budgets be determined. This is essential to derive an unbiased census of the star formation rate density with redshift and thus determine the 'formation epoch' of galaxies (e.g. Blain et al. 1999; Murphy et al. 2011).

Undertaking submillimetre observations from ground-based observatories has always been fraught with difficulty, since atmospheric transparency is often poor and the high background power and sky emission variability limit the observing sensitivity. Nevertheless, 10–15 m class single-dish telescopes, routinely operating with high efficiency for the past 25 years, have led to enormous advances in our understanding of the formation of galaxies, stars and planets. For example, over the past two decades remarkable discoveries have taken place including the discovery of ultra-luminous high-redshift galaxies responsible for the majority of the far-IR background (e.g. Smail, Ivison & Blain 1997; Hughes et al. 1998), pinpointing cold dense regions in molecular clouds where new stars are forming (e.g. Motte, Andre & Neri 1998; André et al. 2010), and imaging of vast clouds of cold dust around nearby stars believed to be analogues of the Kuiper belt in our Solar system (e.g. Holland et al. 1998; Wyatt 2008).

The submillimetre revolution began in earnest in the late 1990s with the arrival of the first imaging cameras, SHARC (Wang et al. 1996), on the Caltech Submillimeter Observatory (CSO) telescope and the Submillimetre Common-User Bolometer Array (SCUBA; Holland et al. 1999) on the James Clerk Maxwell Telescope (JCMT). However, with two arrays containing only 91 and 37 bolometers, mapping even moderately sized areas of sky (tens of arcminutes across) with SCUBA to any reasonable depth was painfully slow. Bolometer cameras with similar total pixel counts also followed on other ground-based telescopes, such as BOLOCAM (Glenn et al. 1998) and SHARC-II (Dowell et al. 2002) at the CSO, LABOCA (Siringo et al. 2009) on the Atacama Pathfinder Experiment telescope, and the MAMBO cameras (Kreysa et al. 1998) on the Institut de Radio Astronomie Millimetrique 30 m telescope. With existing bolometer technology being non-scalable to more than a few hundred pixels, the next challenge was to develop a way to increase substantially the pixel count by up to a factor of 100. The solution came in the form of new detectors incorporating superconducting transition edge sensors (TESs; Irwin 1995), and the ability to adapt techniques such as high-precision silicon micro-machining to produce large-scale array structures (Walton et al. 2005). Furthermore, Superconducting Quantum Interference Device (SQUID) amplifiers could also be chained together to form a complementary, multiplexed readout system (deKorte et al. 2003). These technology advances meant that cameras of many thousands of pixels became conceivable for the first time, and thus formed the major motivation for the SCUBA-2 project.

SCUBA-2 is a dual-wavelength camera with 5120 pixels in each of two focal planes. A focal plane consists of four separate sub-arrays, each with 1280 bolometers, and butted together to give the full field (as shown in Fig. 1). Both focal planes have the same field of view on the sky and are used simultaneously by means of a dichroic beam-splitter. The instrument operates at the same primary wavelengths as SCUBA, namely 450 μm for the short waveband and 850 μm for the long waveband. SCUBA-2 was delivered from the UK Astronomy Technology Centre (Edinburgh) to the Joint Astronomy Centre (Hilo, Hawaii) in 2008 April with one engineering-grade sub-array at each waveband. The first two science-grade sub-arrays (one for each focal plane) arrived at the JCMT in late 2009, and a period of 'shared risk observing' was undertaken between 2010 February and April. The remainder of the science-grade sub-arrays were delivered in summer 2010 and the first astronomical data with the full array complement were taken in early 2011.

In this paper, Section 2 gives an overview of the instrument design including the optics and cryogenics. Section 3 describes in detail the design, manufacture and testing of the superconducting detector arrays. In Sections 4 and 5, we discuss how the instrument takes data and processes the information into astronomical images. Section 6 describes the rudiments of flux calibration whilst Section 7 presents the initial on-sky performance, including sensitivity and optical image quality. In Section 8, we give an overview of the algorithms used in reducing SCUBA-2 data to produce publication-quality images. Finally, Section 9 illustrates the scientific potential of SCUBA-2 with a selection of early results.

2 INSTRUMENT DESIGN

The opto-mechanical design of SCUBA-2 is driven by two principal requirements: (1) to maximize the available field of view and (2) to provide an ultra-low detector operating temperature in the 100 mK regime. The re-imaging of a large field on to a relatively small detector array (Section 3.1.1), as well as infrastructure limitations at the telescope, results in a complex optical path necessitating some extremely large mirrors (up to 1.2 m across). Furthermore, to minimize power loading on the detector arrays, the last three of the re-imaging mirrors are cooled to temperatures below 10 K. Together with the complex cryogenic system, this leads to a large cryostat, the vacuum vessel of which is 2.3 m high, 1.7 m wide and 2.1 m long, with a pumped volume of 5.3 m^3 and a weight of 3400 kg.

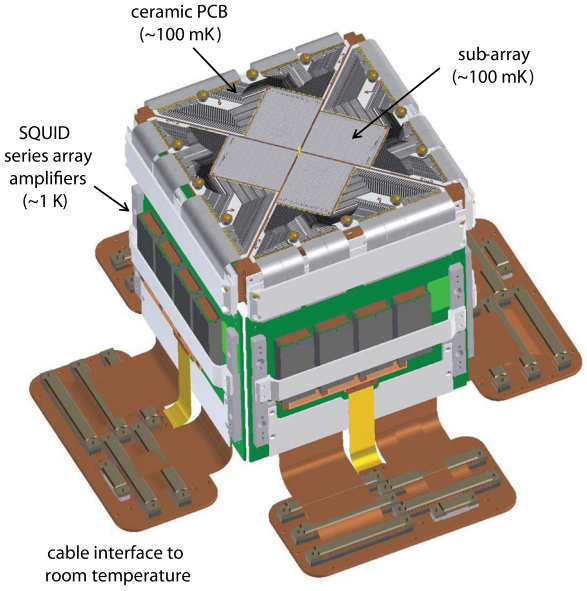

Figure 1. Layout of a SCUBA-2 focal plane unit showing the major components of the assembly. The sub-arrays are butted together, with an approximate 4 pixel gap, to form a focal plane with an approximate 45 arcmin^2 field of view on the sky. The ceramic PCB are wire-bonded to the arrays and these fan out the signal connections to ribbon cables that run to the 1 K amplifiers and eventually via additional cables to room temperature.

2.1 Optical design

Early designs clearly showed that it was not possible to accommodate SCUBA-2 in the JCMT 'receiver cabin' close to the Cassegrain focus. The left-hand Nasmyth platform (as viewed from the rear of the telescope), previously home to SCUBA, was a more realistic location in which the unvignetted field of view of the JCMT is ∼11 arcmin in diameter, restricted by the aperture of the elevation bearing. Given that the focal plane has a square geometry (as dictated by the array manufacturing process), a maximum field of 8 × 8 arcmin was possible. Hence the SCUBA-2 optics re-image the field at the Cassegrain focus to a size compatible with the focal plane footprint at the arrays. To maximize the sensitivity of the instrument and provide excellent image quality this has to be achieved with high efficiency and minimum field distortion. The optics are also designed to ensure that a high-quality pupil image of the secondary mirror is produced at a cold-stop within the cryostat thereby minimizing 'stray light' that could potentially degrade detector sensitivity. Subsequent changes to the array size (Section 3.1.1) restricts the final field of view to ∼45 arcmin^2.

The detailed optics design and manufacture of the re-imaging mirrors are described by Atad-Ettedgui et al. (2006). Referring to Fig. 2, the design consists of a tertiary mirror located in the receiver cabin just above the nominal Cassegrain focus. At the exit of the cabin a relay of three mirrors (labelled C1–C3) re-images the telescope focal plane at a point just beyond the elevation bearing on the Nasmyth platform, thereby converting the $f/12$ telescope beam to $f/7$. A second relay (N1 and N2) re-images the focal plane at $f/2.7$ just inside the instrument, thereby allowing for a small cryostat window diameter. The cold optics, consisting of a further three mirrors (N3, N4 and N5), forms an approximate 1:1 system that re-images the focal plane at $f/2.7$ on to the detector arrays.

The mirrors were manufactured by TNO Science and Industry[1] to have complex free-form surfaces that provide sufficient degrees of freedom to optimize the optical design. This proved necessary to maintain a high Strehl ratio across the field as a function of telescope elevation, as well as minimum field distortion. Packaging the optics within the overall structure of the telescope results in a cryostat location just below the existing Nasymth platform and tilted at an angle of 22° to the vertical. This required a large amount of infrastructural changes at the telescope, as documented in Craig et al. (2010). The overall optical path length is ∼20 m from the tertiary mirror to the arrays. An alignment accuracy of ±0.25 mm, well within acceptable tolerances, is achieved in all axes using an optical datum positioned in the bearing tube (Craig et al. 2010).

2.2 Wavelength of operation

Submillimetre observations from ground-based sites are restricted to wavebands within transmission windows in the atmosphere. For a good observing site such as Mauna Kea, these windows extend from 300 μm to 1 mm and throughout the region atmospheric water vapour is the main absorber of radiation from astronomical sources. The selection of observing wavelength is made by a bandpass filter which, as shown in Fig. 3, is carefully tailored to match a particular transmission window. For SCUBA-2, these are multilayer, metal-mesh interference filters (Ade et al. 2006), located just in front of the focal planes, and have excellent transmission (typically peaking around 80 per cent) and very low (<0.1 per cent) out-of-band power leakage. The half-power bandwidths of the bandpass filters are 32 and 85 μm at 450 and 850 μm, respectively, corresponding to $\lambda/\Delta\lambda \sim 14$ and 10.

A decision was made early in the design to conservatively filter the instrument. Hence there are a series of thermal and metal-mesh edge filters (Tucker & Ade 2006) to ensure that heat loads and stray light are kept to a minimum in such a large instrument. Fig. 4 shows the position of all the filters within SCUBA-2, including the dichroic that reflects the shorter wavelengths and transmits the longer. The addition of extra low-pass edge filters at 4 and 1 K is not a large penalty compared with potentially having to track down stray light sources that could mar image quality, or contending with additional heat loads that could degrade sensitivity. For example, at the entrance of the 4-K optics box it is necessary to keep the thermal power to a minimum to prevent heating of the optics and possible subsequent loading of the 1 K stage. To ensure good frequency selection low-pass edge filters are also used with the bandpass filters. The net transmission of the instrument, in both wavebands and including the cryostat window and the detector absorption efficiency, is ∼40 per cent.

2.3 Main instrument

The cryostat is made up of a series of sub-systems (see Fig. 2) and is designed with nested radiation shields and baffles to minimize stray light and magnetic fields. For example, the arrays themselves contain SQUID amplifiers (Section 3.2.2) that are sensitive magnetometers and so must be shielded from magnetic fields. Immediately inside the vacuum vessel is a high magnetic permeability

[1] TNO Science and Industry, Opto-Mechanical Instrumentation, Precision Mechanics Department, Stieltjesweg 1, P. O. Box 155, Delft, the Netherlands.

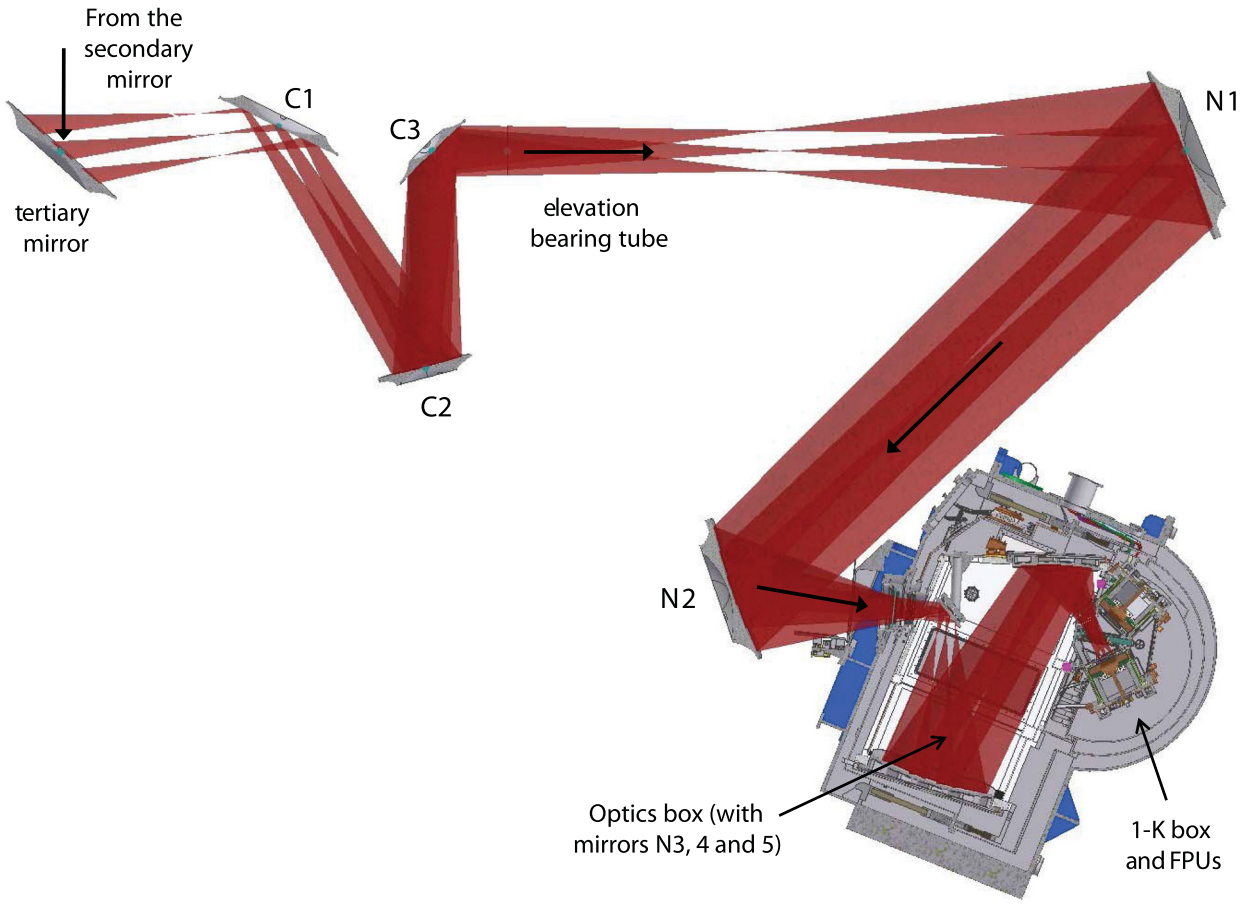

Figure 2. Optical layout for SCUBA-2 from the tertiary mirror to the detector arrays inside the cryostat. The beam envelope, shown in red, is a combined ray trace of the on-axis and two extremes of the field of view for this projection of the optics. The arrow shows the direction of light propagation. Mirror N3 is located just inside the cryostat window, whilst mirrors N4 and N5 relay the optical beam into the array enclosure ('1-K box') which houses the focal plane units (FPUs).

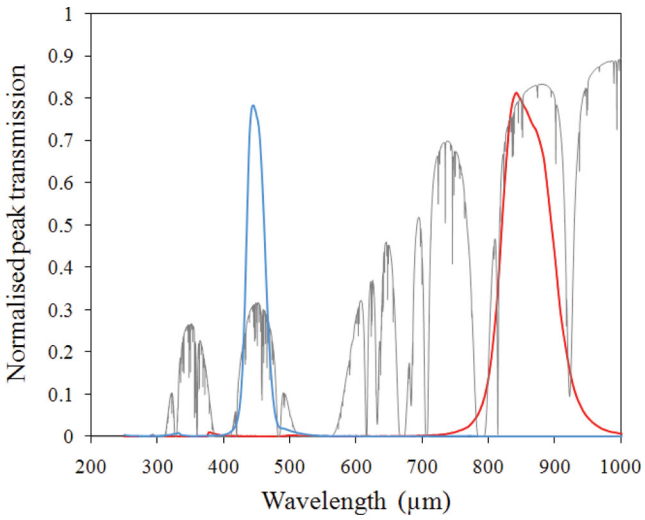

Figure 3. The measured SCUBA-2 bandpass filter profiles at 450 (blue curve) and 850 μm (red), superimposed on the atmospheric transmission curve for Mauna Kea for 1 mm of precipitable water vapour (PWV; grey curve). The atmospheric transmission data are provided courtesy of the Caltech Submillimeter Observatory.

shield, a multilayer insulation blanket and a radiation shield operating at ∼50 K. These provide radiation shielding for the main optics box, that houses the cold re-imaging mirrors at ∼4 K. The radiation shield and optics box are cooled by a pair of pulse-tube coolers (Section 2.5). The main optics box provides the support for the three cold mirrors and the 1 K enclosure ('1-K box'). Mounted within the 1-K box are the two focal plane units (FPUs) that contain the cold electronics and the detector arrays. The still and the mixing chamber of a dilution refrigerator (DR) cool the 1-K box and arrays, respectively (Section 2.5). The 1-K box and the outer casing of each FPU are also wrapped in superconducting and high magnetic permeability material (Hollister et al. 2008a; Craig et al. 2010).

2.4 1-K box and focal plane units

The removable 1-K box creates the required environment for the detector arrays (Woodcraft et al. 2009). In addition to radiation shielding, it provides a cold-stop aperture at the entrance to help minimize stray light. Furthermore, it gives mechanical support for magnetic shielding, a cold shutter (used to take dark frames), filters and the dichroic that splits the incoming beam on to the two focal planes. The 1-K box consists of an outer shell with aluminium alloy panels that hold the high-permeability material for magnetic

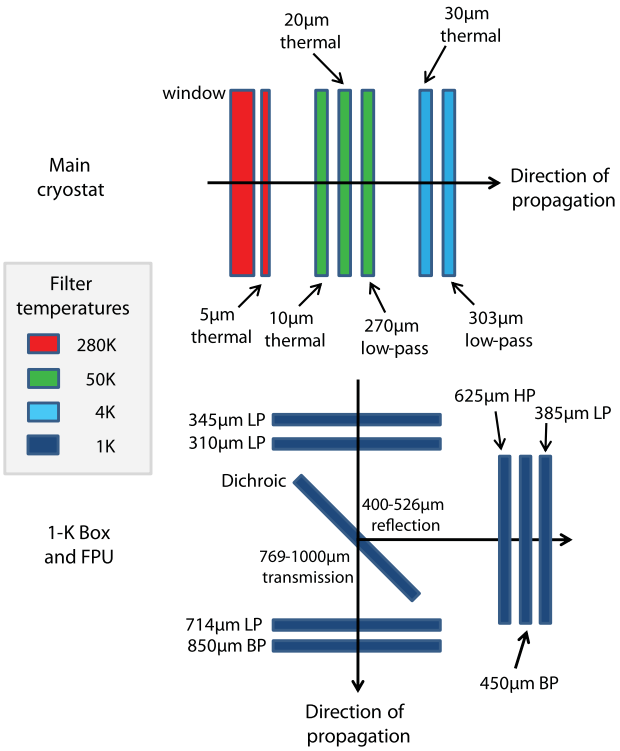

Figure 4. The arrangement and operating temperature (colour coded) of the bandpass (BP), thermal blocking and metal-mesh edge filters and dichroic in SCUBA-2. Top: the main cryostat; bottom: the 1-K box and focal plane units. 'LP' and 'HP' represent low-pass and high-pass filter cut-off edges, respectively. Thermal edge filters reject power shortward of their wavelength cut-off.

shielding (Hollister et al. 2008a). In addition, the box accurately and reproducibly supports and positions the FPUs with respect to the cold-stop. Fig. 5 (left) shows a 3D CAD drawing of the box, highlighting the main components. There are two separate FPUs, each containing four sub-arrays (Section 3.1.1). Key elements of the FPU design include the thermal link to the DR, optical filtering and further magnetic shielding. The 1-K box is a separate sub-system and interfaces to the main cryostat assembly via a support frame. Fig. 5 (right) shows a photograph of the fully assembled 1-K box during installation into the instrument.

2.5 Thermal design and cryogenics

The overall thermal design of SCUBA-2 is described by Gostick et al. (2004). In summary, two Cryomech[2] PT410 pulse-tube coolers keep the radiation shields and the ∼300 kg of cold optics at 50 and 4 K, respectively. However, since their cooling power is insufficient for the initial cool-down phase on a reasonable time-scale, pre-cool tanks are attached to the 50 and 4 K shields. After pre-cooling with liquid nitrogen (LN_2) the instrument is kept cold without the need for any liquid cryogens in the main instrument. A modified Leiden Cryogenics[3] DR was commissioned to run with a pulse-tube cooler (PT410) and Joule–Thompson heat exchanger, eliminating the need for a conventional 1-K pot and liquid cryogens. The still of the DR cools the 1-K box, whilst the mixing chamber cools the ∼30 kg of focal planes to around 100 mK. The DR is a key element of the system and has to cope with a substantial thermal load from the arrays themselves, heat leaks down the mechanical array supports and wiring, as well as radiation loading from the warmer parts of the instrument, telescope and sky (Hollister et al. 2008b). The thermal design is complex, with the need to transfer cooling power at temperatures of 1 K and 100 mK over a distance of 1.5 m to various locations in the FPUs, and to support the arrays rigidly whilst keeping sufficient thermal isolation to the 100 mK stage. A large number of thermal links are therefore required, with the added need for several bolted interfaces to allow the FPUs to be removed from the instrument. Nevertheless, with the benefit of extensive thermal modelling, the instrument reached the required cryogenic performance on the first cool-down. Under a total thermal load of 70 μW the mixing chamber of the DR achieves a base temperature of 70 mK in regular operation (Bintley et al. 2012a).

Early operation on the telescope revealed two main problems. The first was that the DR was prone to blocking after only 4–5 weeks of continuous operation. This was due to a gradual build-up of contamination not removed by the LN_2 cold traps, which over time causes a blockage, most likely in the flow impedance of the cold insert. An additional external 4 K cold-trap (cooled by liquid helium) significantly extended the run-time, allowing the instrument to remain cold for more than six months continuously. The second issue was that a very distinct oscillation (period ∼25 s) was seen in the bolometer output signals. This was traced to a temperature oscillation originating in the still of the DR. The oscillation is a result of both tilting the DR to 22° and the strong interaction between the still and the circulation of ^{3}He gas (this being a consequence of using the still to condense the gas as part of the new DR design; Bintley et al. 2012a). A new temperature control system on both the support structure underneath the arrays and 1-K box minimized the amplitude of the oscillation. The temperature fluctuations have been reduced by at least a factor of 10, to ±20 μK at the array supports. Under temperature control the mixing chamber achieves a base temperature of 78 mK.

3 DETECTOR ARRAYS

3.1 Requirements

3.1.1 Pixel count and array geometry

To fully Nyquist sample the sky instantaneously, the detector spacing must be $0.5f\lambda$, where f is the final focal ratio of the optics. With $f/2.7$ this corresponds to a spacing (and approximate detector diameter) of 0.61 and 1.14 mm at 450 and 850 μm, respectively. To cover the maximum available field of view requires approximately 25 600 and 6400 bolometers for the two wavebands. Early design work showed that there was an approximate 1.1 mm minimum constraint on the size scale of the multiplexer (MUX) unit cell, rendering a fully sampled 450 μm focal plane impractical. The detector size and spacing was therefore relaxed to $\sim f\lambda$ at 450 μm producing an array that undersamples the sky by a factor of 4, leading to a subsequent reduction in mapping speed (Section 7.3). However, this decision greatly simplified the fabrication process, since the MUX wafers became identical at the two wavelengths (Section 3.2.2). Furthermore, fabrication limitations meant that the maximum size of an individual detector or MUX wafer was 50 mm^2, and hence the focal planes are populated with four separate quadrants, or sub-arrays. Finally, the need for space on the MUX wafer for wire-bond pads, extra

[2] Cryomech, 113 Falso Drive, Syracuse, NY 13211, USA.
[3] Leiden Cryogenics BV, Galgewater 21, 2311 VZ Leiden, the Netherlands.

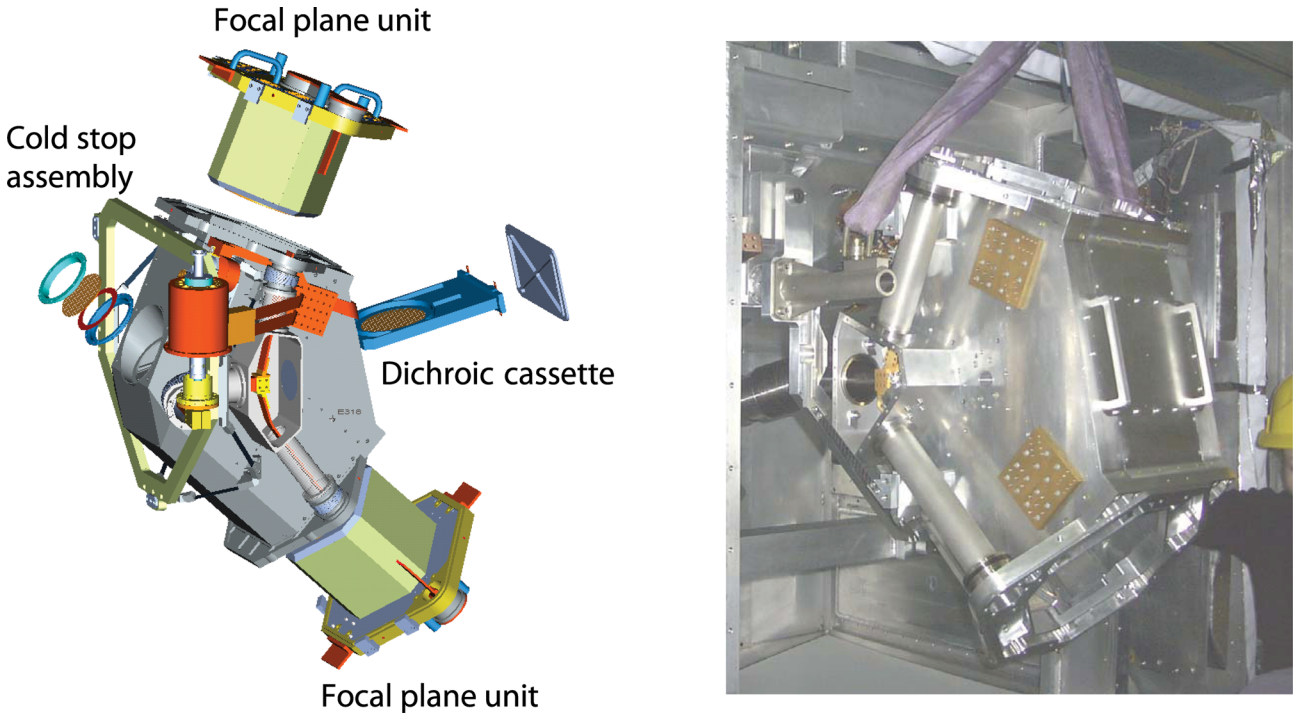

Figure 5. Left: 3D CAD drawing of the 1-K box showing the main components of the focal plane units, cold-stop assembly and dichroic cassette. The shutter, not shown in this drawing, is located in front of the cold-stop on the outside of the 1-K box. Right: photograph of the fully assembled 1-K box during installation into the main SCUBA-2 cryostat.

bump-bonds, and the second stage SQUID configuration, means that the size of a sub-array is further restricted to 32 columns by 40 active rows (Section 3.2.2).

3.1.2 NEP and power handling requirements

The key performance requirements for the detectors are the bolometer noise (or noise equivalent power, NEP; Section 3.5.2), the power handling capability (saturation power) and the speed of response (time constant). The fundamental requirement is that the overall SCUBA-2 sensitivity be limited by the background photon noise due to sky, telescope and instrument, under all observing conditions. A detailed model, based on the heritage of SCUBA, was constructed to allow the background power levels and performance figures to be established. As shown in Table 1, the 450 μm bolometers have to cope with larger sky power levels than their 850 μm counterparts, and under the driest observing conditions the background power is approximately 10 times less at 850 μm than at 450 μm. The specification of the total power handling capability therefore takes this into account, and also has to include additional margin for electrical TES bias and the calibration heater power (Section 3.4.1). In terms of the NEP, the 850 μm waveband sets the most stringent requirement as the sky background power is considerably lower than at 450 μm. The minimum background-limited NEPs (NEP_{bkg}) are 2.7×10^{-16} and 5.6×10^{-17} W $s^{1/2}$ at 450 and 850 μm, respectively. Hence, the intrinsic NEP of a bolometer must be less than these values to be background limited. For an ideal TES bolometer, measured in the absence of background power, phonon noise dominates the NEP at low frequencies (Section 3.2.1). Hence, the specification adopted for SCUBA-2 is that the phonon noise limited NEP for an individual bolometer is $<0.5 \times NEP_{bkg}$. Given that the NEP will be degraded by additional noise in the readout circuit the formal specification is that the measured *dark* NEP (i.e. measured in the absence of

Table 1. Summary of the predicted power levels under the best and worst atmospheric conditions, and the per-bolometer requirements in terms of power handling, NEP, transition temperature, thermal conductance and time constant. The minimum background power is estimated in the best observing conditions for which zenith sky transmissions of 40 and 85 per cent at 450 and 850 μm have been adopted. For the maximum power levels transmission values of 3 and 40 per cent have been used.

Parameter	Units	450 μm	850 μm
Minimum background power	(pW)	70	7
Maximum background power	(pW)	120	16
Total power handling/saturation power	(pW)	230 (±10 per cent)	50 (±10 per cent)
Minimum background NEP	(W $s^{1/2}$)	2.7×10^{-16}	5.6×10^{-17}
Detector (phonon) noise limited NEP	(W $s^{1/2}$)	$<1.35 \times 10^{-16}$	$<2.8 \times 10^{-17}$
Measured dark NEP	(W $s^{1/2}$)	$<1.9 \times 10^{-16}$	$<4.0 \times 10^{-17}$
Transition temperature (T_c)	(mK)	190 (±5 per cent)	130 (±5 per cent)
Thermal conductance (G)	(nW K^{-1})	4.2 (±5 per cent)	1.3 (±5 per cent)
Time constant	(ms)	< 1.5	< 2.8

background power) is $< 0.7 \times \mathrm{NEP_{bkg}}$. These values are summarized in Table 1.

3.1.3 Frequency response

SCUBA-2 is designed to conduct large-area surveys by scanning the telescope in a rapid, overlapping pattern (Section 5.1). If the detector response is too slow, some of the higher spatial frequencies in the science signal will be attenuated. The telescope acts as a spatial filter, since the measured response is the convolution of the response of the astronomical signal and the telescope beam. The maximum frequency present in the system response is given by $v_{\mathrm{tel}}/(pf\lambda)$, where v_{tel} is the telescope scanning speed and p the plate scale (5 arcsec mm^{-1}). Since the telescope can scan at speeds up to 600 arcsec s^{-1} with high positional accuracy, resulting data will therefore have maximum frequencies present of 100 and 50 Hz at 450 and 850 μm, respectively. Thus the detector time constants must be $<$1.5 and $<$2.8 ms to avoid significant attenuation of the signal during fast scanning. More details of the derivation of the detector and array requirements are given in Hollister (2009).

3.2 Design and fabrication

The SCUBA-2 sub-arrays are based on TESs and time-division SQUID-based MUXs developed at the National Institute of Standards and Technology in Boulder, Colorado (Irwin & Hilton 2005). The superconducting elements themselves are formed from a molybdenum/copper (Mo/Cu) bilayer of material, the relative thickness of each layer determining the superconducting transition temperature. The geometry of each sub-array is 32 columns by 40 active rows of bolometers. As shown in the schematic diagram of a single bolometer in Fig. 6, each sub-array consists of two separate wafers, fabricated separately and then hybridized together.

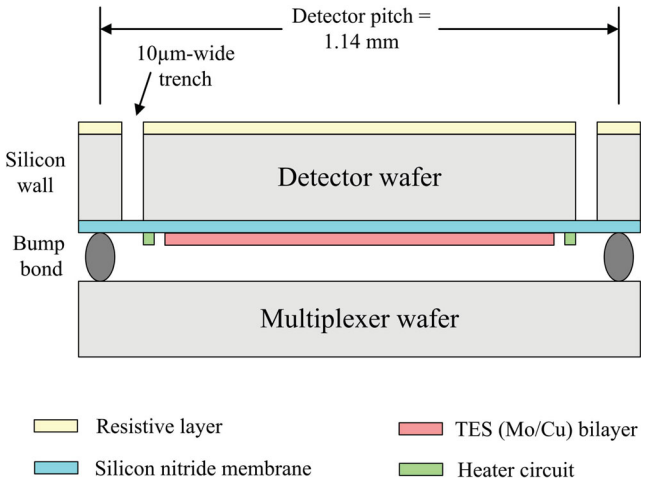

Figure 6. A schematic representation of a single SCUBA-2 bolometer showing the principal components. These include the absorbing resistive layer on the top of the detector wafer and the deep trenches that thermally isolate each bolometer from their neighbours. The TES bilayer sits between the silicon nitride membrane and the bottom of the detector wafer. The heater circuit runs around the edge of each bolometer and is used for calibration. The MUX wafer containing the SQUID amplifier circuitry is indium bump-bonded to the detector wafer. Note: diagram is not to scale.

3.2.1 Detector wafer

The 'detector wafer' upper surface is implanted with phosphorus ions to provide an absorbing layer to incoming electromagnetic radiation, whilst the Mo/Cu bilayer on the lower surface forms a highly reflective backshort. For efficient radiation absorption the thickness of the wafer is made equal to an odd number of quarter wavelengths, 3λ/4 at 450 μm and λ/4 at 850 μm (Audley et al. 2004). An underside silicon nitride membrane mechanically supports each TES bolometer on the wafer and provides a weak thermal link to the cold bath. For ease of manufacture the sub-arrays for 450 and 850 μm are identical, except for the aforementioned thickness of the detector wafer. The final part of the detector wafer design is a heater circuit arranged in a thin-line geometry around the edge of each bolometer (Section 3.4.2). In terms of fabrication, and to ease handling, a second silicon wafer is fusion bonded to the upper surface of the detector wafer (after the implantation stage). This is eventually removed after hybridization with the MUX wafer, just prior to the post-processing step that thermally isolates each bolometer via a deep-etched 10 μm wide trench to the silicon nitride layer (Section 3.2.3).

The detector operating temperature and thermal conductance of the link to the cold bath govern the theoretically achievable NEP, according to $\mathrm{NEP_{phonon}} = \sqrt{4\gamma k_{\mathrm{B}} T^2 G}$, where T is operating temperature (approximated by the superconducting transition temperature, T_{c}), G the thermal conductance and γ is a factor that accounts for the temperature gradient across the silicon nitride membrane (assumed to be 0.7 in this case; Mather 1982). Target values of T_{c} and G are chosen to provide background limited performance, and also to contend with varying degrees of power as the sky emission changes. As discussed in Section 3.1.2 the 850 μm waveband sets the most stringent requirement in terms of NEP. In addition, to minimize sensitivity to temperature fluctuations T_{c} should be roughly twice the expected base temperature. At 850 μm the value of T_{c} is therefore set to 130 mK. At 450 μm, where the sky power is higher, T_{c} can also be made higher, in line with the relaxed NEP requirement. Strictly, only a value of 380 mK is needed to ensure the 450 μm waveband is background limited. However, given the desire to keep the array fabrication common to both wavebands, and that a 100 mK operating temperature regime is needed in any case for 850 μm, a T_{c} of 190 mK was adopted at 450 μm, thereby giving even more margin on the required NEP. The value of G is given by $G \sim (nP)/T$, where P is the saturation power and n is a power-law constant, which is typically 3.5 for silicon nitride membranes. Hence, the required values of G are 4.2 and 1.3 nW K^{-1} at 450 and 850 μm, respectively. The target T_{c} and G values are given in Table 1.

3.2.2 Multiplexer wafer

The bottom of 'multiplexer' wafer contains the input coupling coils and SQUID amplifiers of the readout circuit (as shown in Fig. 7). Current flowing through the TES generates a magnetic field at the first stage SQUID (SQ1) through an input transformer on the wafer (the details of which are not shown in Fig. 7 for clarity). Each column of SQ1s is then coupled by a summing coil to the second stage SQUID (SQ2). The signals are amplified by a SQUID Series Array (SSA) that has 100 SQUIDS in series per channel and is located on the 1 K printed circuit board (PCB) of the cold electronics module (see Section 3.3). The MUX wafer is designed with 41 rows with the first row being a 'dark row', without any corresponding TES element but containing a SQ1. The output of the dark row has been used to

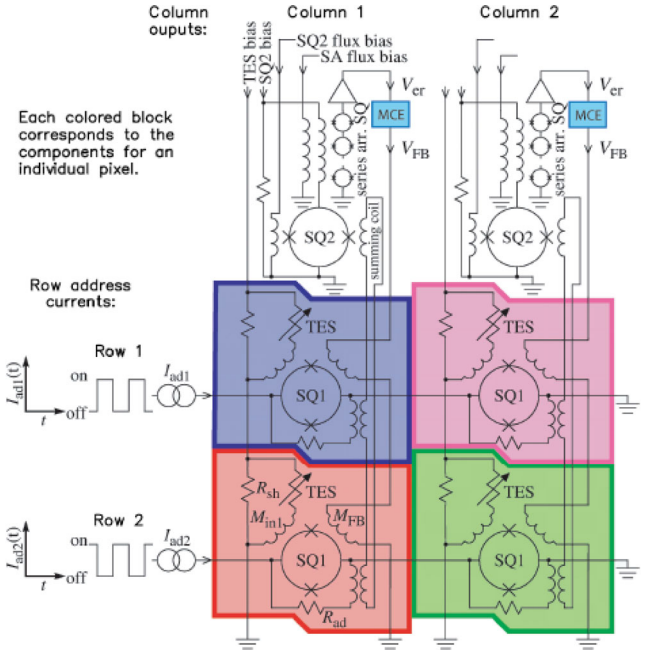

Figure 7. A two-column, two-row schematic representation of the SQUID time-division multiplexed readout scheme for SCUBA-2 (Doriese et al. 2007). Each TES is inductively coupled to its own first stage SQUID (SQ1). A summing coil carries the signals from the SQ1s in a column to a common second stage SQUID (SQ2). The rows of SQ1s are sequentially switched on using an address current (I_{ad}), so the signal from one TES at a time (per column) is passed to the SQ2. Finally, the output of each SQ2 is passed to a 100 SQUID series array (SSA) amplifier and then to the room temperature electronics (MCE).

investigate common-mode noise on a per-column basis, but is not currently implemented by default in the data reduction software. It is the SQUID MUX that makes large-scale TES arrays, such as SCUBA-2, practical by vastly reducing the wire count between the detectors and the room temperature electronics (deKorte et al. 2003). The SCUBA-2 MUX design reduces the wire count from 82000 to 2700 – a MUX factor of approximately 30. The MUX wafers are independently tested prior to hybridization with the detector wafer, using a dedicated facility at the University of Waterloo that measures yield and critical currents (I_c) of the MUX wafers. Testing at this stage allows fabrication faults to be identified and corrected.

3.2.3 Hybridization and post-processing

The detector and MUX wafers are hybridized together using a low-temperature indium bump-bonding process developed at Raytheon Vision Systems.[4] The bump-bonds provide both thermal and electrical contact between the two wafers. There are 74 bumps surrounding each detector element (including four bumps that make the electrical connection between wafers for the bias and heater) and a further 100 000 bumps per sub-array around the perimeter of the wafers to give extra mechanical support. The first step of post-processing is to etch away the 'handle wafer' to the level of the implanted absorbing layer. This is followed by thermally isolating each individual bolometer by deep etching a trench in the main detector wafer to the silicon nitride membrane (see Fig. 6; Walton et al. 2005). The trenches are 10 μm wide and either 60 or 100 μm deep depending on the thickness of the detector wafer (Section 3.2.1). Maintaining this width at the bottom of the trench across the entire sub-array is critical as this (largely) controls the value of G. At this stage a final electrical continuity check allows any remaining fabrication issues to be repaired (such as electrical shorts that may have been introduced in the hybridization process). The final step in the array processing is to laser dice the circular wafer assembly into the final rectangular sub-array geometry.

[4] Raytheon Vision Systems, 74 Coromar Drive, Goleta, CA 93117, USA.

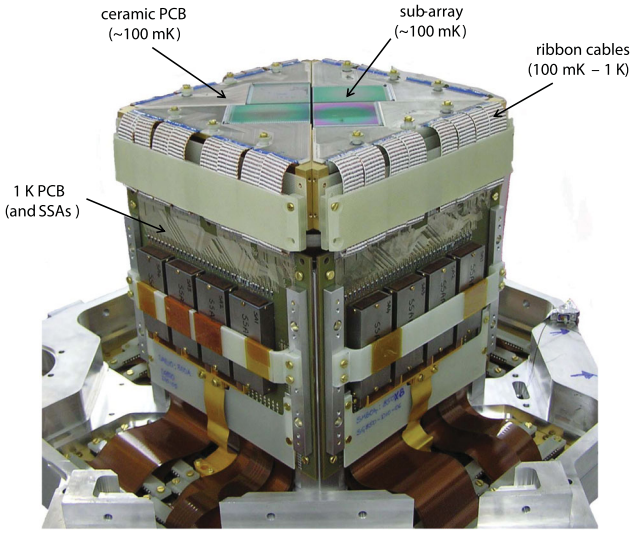

Figure 8. Photograph of four sub-array modules folded into position in a focal plane unit. The principal components are highlighted.

3.3 Array integration

Completed sub-arrays are packaged as stand-alone modules that are mounted in the focal plane of the instrument. The sub-array is first epoxy-bonded on to an array support holder. As thermal conduction laterally through the sub-array is poor, the holder needs to make thermal contact to the entire back surface of the sub-array to provide sufficient cooling. The holder must also be made from a metal for effective thermal conduction, but this results in a large mismatch in thermal contraction between the holder and the (largely silicon) sub-array. The array holder is therefore designed in the form of a beryllium–copper block in which individual spark-eroded tines make contact with the underside of the MUX wafer through an epoxy bond, with the pitch of the tines being identical to that of the MUX unit cells. By allowing for differential thermal contraction during cooling damage to the sub-array is avoided. Once attached to this 'hairbrush' array holder the sub-array is integrated into the 'sub-array module', making electrical connection to a ceramic PCB (see Fig. 1) through aluminium wire bonds. Phosphor bronze–clad niobium titanium (NbTi) wires, woven into Nomex® cables (manufactured by Tekdata Interconnections[5]), carry the signals from the ceramic PCB to a 1 K PCB, that houses the magnetically shielded SSAs. Further woven ribbon cables (monel-coated NbTi) take the signals to the warm electronics on the outside of the cryostat. The design of both sets of cable is critical to minimize any heat leaks from either 1 K or higher temperatures. Fig. 8 shows a photograph of four sub-array modules folded into position in an FPU.

[5] Tekdata Interconnections Ltd., Innovation House, The Glades, Festival Way, Etruria, Stoke-on-Trent, Staffordshire ST1 5SQ, UK.

3.4 Array operation

3.4.1 Sub-array setup and bias optimization

Before operation can begin the arrays must be setup in their optimum configuration. This process has three main steps, the first two of which are performed quite rarely as the parameters are fixed and unlikely to vary with time (at least on a per cool-down basis). The first stage is called 'full array setup' and refers to the process of determining the optimal SQUID bias for each level of SQUIDs. It sets the SSA bias to I_c(max) for maximum modulation, second stage SQUID bias to 1.5–2 I_c(max) for optimal bandwidth, and the first stage SQUID bias to the mode value of the 32 bias settings that gave maximum modulation of the SQ1 for each row. The second stage or 'detector setup' refers to the process of selecting the optimal TES bolometer and heater biases for each array. This involves sweeping out the available parameter space and selecting operating values such that the NEP across a sub-array is minimized. The final step, and the one that is performed regularly, is 'fast array setup' and refers to the process of determining the flux offsets for each level of SQUIDs with the SQUID, TES and heater biases set to their nominal operating values. The array setup process is more fully described in Gao et al. (2008).

3.4.2 Heater tracking

One of the innovative features of SCUBA-2 is the inclusion of a resistive heater arranged around the edge of every bolometer. The heaters play a fundamental role in the operation during observing in that they are used to compensate for changes in optical power as the sky background changes, enabling the TES bias point to be constant for a wide range of sky powers. Furthermore, each bolometer is individually calibrated by measuring its responsivity using a small ramp of the heater current (Section 5.2). The optical power from the sky is directly measured using a process called 'heater tracking'. This involves running a servo loop on the heater to keep the bolometer output constant while opening and closing the cold shutter to the sky. Periodic heater tracking transfers the slow changes in sky power to the heater setting, thereby maintaining the optimal power balance in a bolometer as determined during the array setup. The absolute level of power depends on the heater resistor values. In practice the average heater current from approximately 100 of the most stable bolometers on a sub-array are monitored. Although the resistors are nominally 3 Ω, all the power from the resistors is not necessarily coupled to the TES film. Thus each sub-array has a 'heater coupling efficiency factor' (Section 3.5.1) to ensure that the responsivity and hence the NEP (Section 3.5.2) is well calibrated.

3.4.3 Sub-array operation

The SCUBA-2 TES bolometers are operated in an approximate voltage-biased mode using a small 5 mΩ shunt resistor (R_{sh}) located on the MUX wafer (as shown in Fig. 7). The advantage of voltage biasing the TES is that negative electro-thermal feedback (ETF) stabilizes the bolometer against thermal runaway. An increase in background power warms the device and causes an increase in resistance, which in turn causes the bolometer current to decrease, thereby cooling the TES. Strong ETF essentially keeps the temperature of the TES constant, while providing a simple and direct relation between any applied power (optical or heater) and the current flowing through the device. Negative feedback also makes the bolometer self-biasing in terms of temperature in the transition. Variations in the incident power are automatically compensated for by changes in the bias current power on time-scales shorter than the time-constant of the bolometer and via the heater for longer-term drifts (Section 3.4.2). As with all such devices, with too much applied power (optical, thermal or electrical bias) the TES becomes normal and ceases to work as a bolometer, and with too little applied power the TES becomes superconducting, with the same effect.

The current flowing through each TES element is measured by its own first stage SQUID (SQ1). The output of a SQUID is periodic with magnetic flux from the input coil, the periodicity being given by a flux quantum (deKorte et al. 2003). Since there is no unique output for a given detector current the SQ1 is used as a null detector. Current is applied by the room temperature electronics (Section 4.1) to the SQ1 feedback coil to null the field from the TES current in the input coil. By applying a flux locked loop, the applied feedback current is proportional to the current flowing through the TES. The dynamic range of the detector feedback circuit is limited by the available first stage SQUID feedback current and the mutual inductance of the SQ1 input coil. These parameters are carefully chosen to meet the stringent noise requirements of the instrument.

3.5 Sub-array performance

The first two science-grade sub-arrays were tested individually in a dedicated cryostat at Cardiff University (Bintley et al. 2010). All of the sub-arrays were then either re-tested or tested for the first time in the SCUBA-2 instrument at the telescope. This aimed to characterize the sub-array performance initially under dark conditions (i.e. with the shutter closed; as presented in this section) and then on the sky under observing conditions (Section 7.2). The power leakage around the shutter when closed is small (<0.5 pW) compared with, for example, a minimum sky power of ∼7 pW at 850 μm.

3.5.1 Thermal and electrical characteristics

As discussed in Section 3.2.1 the operating (and transition) temperature and the thermal conductance to the cold bath dictate the achievable detector NEP and control the total power handling capability. The measurement of T_c and G starts with the bolometers in the normal state. The heater current is gradually reduced until the TES passes through its transition, with a small amount of bias power helping to identify the start of the transition. This process is then repeated at different temperatures. The measurement technique requires an accurate calibration of the heater resistance. As discussed in Section 3.4.2, the 'effective' heater resistance will be lower than the design value because of the imperfect coupling between the heater and the TES element, and inevitably some heat will flow into the walls between bolometers. The effective resistance is determined from a series of *I*–*V* curves at different heater settings. The response of each sub-array is then normalized by a 'heater coupling efficiency' factor based on optical measurements performed with ambient and LN_2 temperature loads at the window of the cryostat and by observation of standard calibration sources (Section 6.2). This ensures that each sub-array reports equal power when observing the same source. Table 2 gives the mean T_c and G across each of the eight sub-arrays. The detector time constants are measured by applying a square wavefunction to the heater and measuring the bolometer response using a fast readout mode available with the room temperature electronics. The measured time-constants are typically 1 ms.

Table 2. The measured thermal and electrical properties of the SCUBA-2 science-grade sub-arrays, including a comparison of the expected phonon noise limit with the measured NEP in the dark. The naming convention for the sub-arrays is s4a, s4b, s4c and s4d for the 450 μm focal plane, and s8a, s8b, s8c and s8d at 850 μm.

Sub-array name	Measured G ($\mathrm{nW\,K^{-1}}$)	Measured T_c (mK)	Phonon-limited NEP ($\mathrm{W\,s^{1/2}}$)	Saturation power (pW)	Measured dark NEP ($\mathrm{W\,s^{1/2}}$)	Yield (per cent)
s4a	4.9	212	9.2×10^{-17}	328	3.2×10^{-16}	84
s4b	6.1	206	1.0×10^{-16}	356	2.7×10^{-16}	72
s4c	8.5	203	1.2×10^{-16}	541	4.6×10^{-16}	65
s4d	6.1	198	9.6×10^{-17}	372	2.7×10^{-16}	65
s8a	4.3	145	5.9×10^{-17}	162	1.1×10^{-16}	80
s8b	2.8	130	4.3×10^{-17}	87	1.5×10^{-16}	60
s8c	3.7	154	5.3×10^{-17}	162	1.1×10^{-16}	61
s8d	5.7	147	5.8×10^{-17}	238	1.6×10^{-16}	65

Although test 'witness' samples were taken during the T_c deposition processes, the measured values of T_c are, in most cases 8–10 per cent higher than the specification of 190 (±5) and 130 (±5) mK for the 450 and 850 μm bolometers, respectively. The higher-than-expected T_c is not well understood but one possibility is that the wafers suffered from annealing in the processing after the bilayer deposition stage. The variation in T_c on an individual sub-array is mainly radial, with values being lower in the (offset) centre position and typically increasing by 10 per cent towards the edges (Bintley et al. 2012b). This is a consequence of the sputtering process in which the detector wafer spins as the copper and molybdenum are deposited.

The values of G are much higher than the design, typically by factors of 2–3. G tends to be more uniform across the array although there is a slight radial dependence similar to T_c, being smaller in magnitude towards the centre. The reason why G is so much higher than the requirement is not well understood. Sub-array s8b, which was the first one fabricated (a year ahead of the others), appears to be somewhat anomalous in terms of having T_c and G much closer to the specification. G is controlled by the geometry of the silicon nitride membrane and it is known that phonon transport across thin film membranes at very low temperatures is a complex and poorly understood process, and may, for example, depend on factors such as the roughness of the membrane surface. This is a particularly important consideration for the ultra low NEP detectors needed for ground-based Cosmic Microwave Background experiments (where sensitivity is paramount over number of bolometers) and space-borne instruments of the future (where background power levels will be very low). From Table 2 it can be seen that expected phonon noise NEP, based on measured values of G and T_c, is significantly higher than the requirement to ensure background limited performance at 850 μm (Section 3.1.2; Table 1).

3.5.2 Dark NEPs

The noise equivalent power (NEP) is conventionally defined as the signal power that gives a signal-to-noise ratio (S/N) of unity for an integration time of 0.5 s. The dark NEP per bolometer is calculated from the ratio of the measured dark current noise (determined over a frequency range of 2–10 Hz) to the responsivity (calculated from a ramp of the heater current; Section 5.2).[6] Taking simply the mean of the NEP of every bolometer per sub-array would be skewed by poorly performing detectors (as the distribution of values is non-Gaussian and so a weighted mean is used.[7] Since a dark-noise measurement is routinely carried out at the start of every astronomical observation a huge data base of measurements now exists. The values given in Table 2 are a median value of 6 500 dark noise measurements taken between the period 2012 February and 2012 July. The measured dark NEP is typically 2–4 times higher than the expected phonon noise limited NEP. The high NEPs could be due to excess low-frequency noise and/or lower-than-expected responsivities. There are several possible mechanisms to generate excess noise over the 2–10 Hz range, including aliased noise from high-frequency sources and effects due to magnetic flux trapped in the SQUIDs during cool-down (there is some evidence from the dark SQUID data that this could be a significant factor). The SCUBA-2 bolometers also exhibit excess noise at frequencies below 1 Hz with a typical '1/*f*' knee at around 0.7 Hz. Although excess noise mechanisms are still under investigation, the source of 1/*f* noise is believed to be largely intrinsic to the detector itself and not associated with the SQUIDs or readout circuit (based on measurements of the dark SQUID data). This fundamental limitation is the main reason why fast scanning modes have to be developed to move the signal frequencies beyond the 1/*f* knee.

3.5.3 Overall yield and stability

Fig. 9 shows typical dark NEP 'images' for each of the eight sub-arrays and histograms of the NEP distribution. As can be seen, there are a number of non-functional bolometers. Some rows, columns and individual bolometers are faulty as a result of an issue during fabrication and show no response at all (e.g. a broken wire bond or non-functional SQ2 can knock out an entire column). Others are deliberately switched-off in a 'bad-bolometer' mask, if, for example, they show sign of instability (e.g. an oscillating output). As well as the higher-than-expected T_c and G, the variation of these properties across a given sub-array has performance and operational implications. There are some sub-arrays (e.g. s8b and s8d) that show distinct gradients or variations in NEP as a result of this. A single TES and heater bias (per sub-array) is insufficient to overcome these

[6] The SCUBA-2 software calculates noise values for an integration time of 1 s, and so the measured values in Table 2 have been multiplied by $\sqrt{2}$ to allow for a comparison with the theoretical phonon NEP that assumes a post-detection bandwidth of 1 Hz – equivalent to an integration time of 0.5 s, as given by the equation in Section 3.2.1.

[7] The weighted NEP, $\mathrm{NEP_{weight}} = \mathrm{NEP^{-2}\,NEP_{mean}}$.

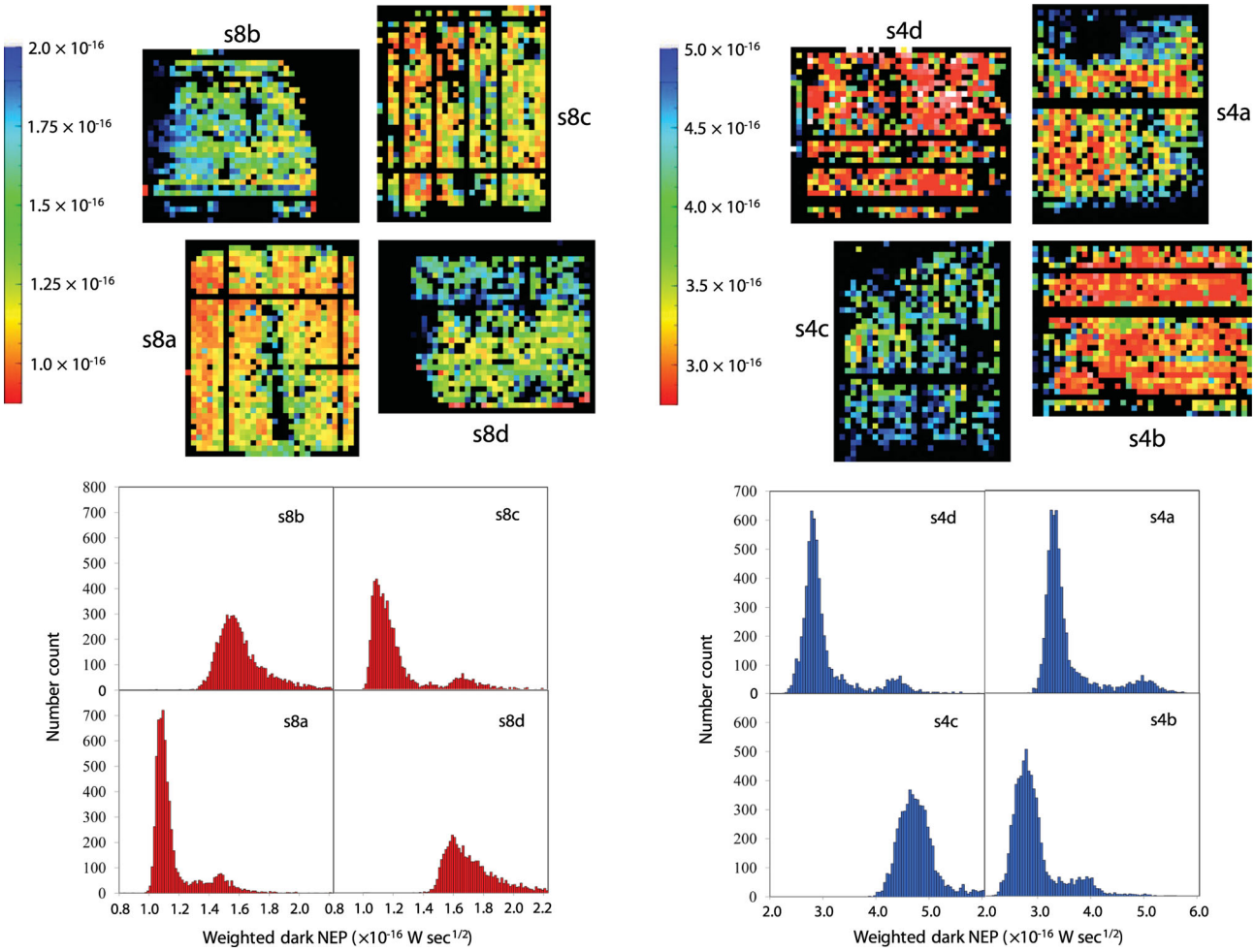

Figure 9. Top: typical dark NEP images recorded with the shutter closed for each of the SCUBA-2 sub-arrays. These are derived from a 'dark noise' measurements of ∼10 s at the start of each observation. The colour scale on each image represents the NEP in units of W $s^{1/2}$. Bottom: dark NEP histograms for each sub-array, each on the same scale for ease of comparison.

variations, resulting in regions of the sub-array where the bolometers are not biased into transition. Furthermore, other bolometers are less than optimally biased in terms of minimum noise and maximum responsivity (i.e. minimum NEP). One possible way to smooth out the effects of the variation in T_c is a novel technique called 'T_c flattening'. By applying a higher SQ1 bias on selected rows for a short period in the MUX cycle, the SQ1 can be used as a secondary heater, thereby allowing rows of bolometers to be more optimally biased. With reference to Fig. 9 this would particularly benefit sub-arrays s8b, s8d and s4a. However, it is a limited technique in that it can only work on a row of bolometers and cannot correct for any T_c variations across a row. At the time of writing this technique remains under investigation and is not currently implemented.

The sub-array yields presented in Table 2 are the typical percentages of bolometers that contribute to an observation [these having been through a flat-fielding quality assurance (QA) test; Section 5.2]. The average yield is about 70 per cent, which was the target goal at the start of the array design and fabrication process. Further QA checks on the bolometers during the map-making process typically reject another 5 per cent of bolometers. The final map yields are therefore typically ∼65 per cent, corresponding to approximately 3700 (out of 5120 bolometers) operational in a focal plane. Whilst minimizing the NEP at the same time as maximizing the yield of a sub-array remains work in progress, the SCUBA-2 working bolometer counts are by far the highest of any submillimetre instrument.

The sub-array stability has significantly improved from the time when the instrument was first installed on the telescope. In the early commissioning phase, bolometers often became unstable during even modest slews of the telescope. This was attributed to pickup in the SQUID summing coil as the sub-arrays bisect the local magnetic field. Additional magnetic shielding in the instrument (Craig et al. 2010) and enhancements to the array setup procedure improved the stability significantly, to such an extent that the majority of bolometers now remain stable during even the largest of scans. As a precaution, regular fast setups are still performed after a lengthy telescope slew. The SCUBA-2 bolometers can show occasional distinct jumps or steps in the time series data, most likely caused by cosmic ray events. The steps are now identified and corrected by an algorithm in the data reduction software (Section 8; Chapin et al. 2013). From repeated measurements it has been shown that the dark performance is usually stable and very repeatable, with less than 5 per cent variation in the dark NEP between successive measurements.

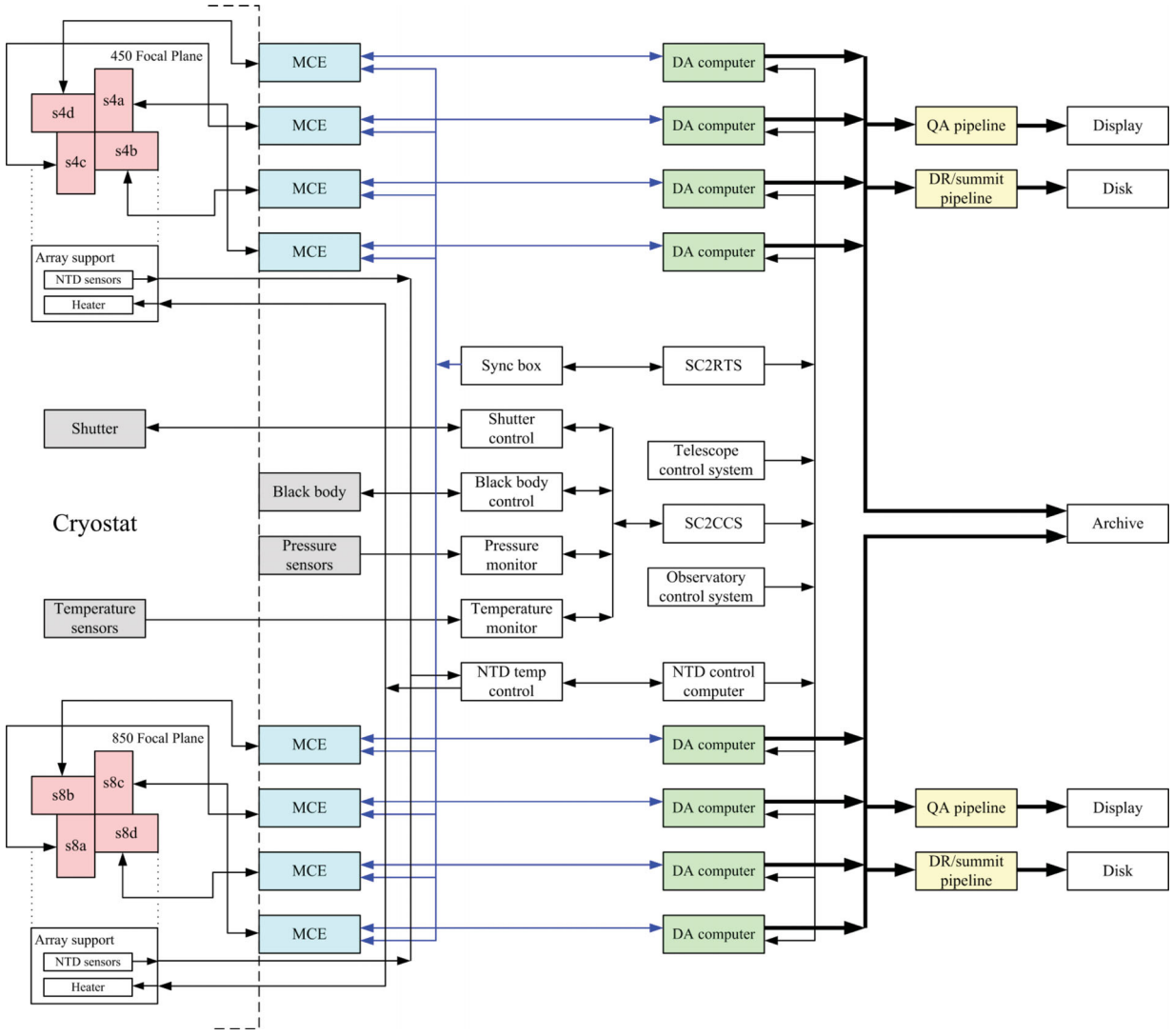

Figure 10. Schematic view of the data flow from the SCUBA-2 bolometer arrays showing the two pipelines running concurrently. The data from each sub-array is handled by a single data acquisition (DA) computer, which the pipelines read from to produce images. See Section 4 for an explanation of the acronyms.

4 SIGNAL AND DATA PROCESSING

The overall signal and data flow for SCUBA-2 are summarized in Fig. 10. This also includes monitoring of the instrument (temperatures and pressures) as well as temperature and mechanism control (SC2CCS). Each sub-array is read out using room temperature electronics (known as multichannel electronics, or MCE) which in turn are each controlled by a data acquisition (DA) computer. The data from the arrays transfer as frames at a rate of approximately 180 Hz and are combined by the data reduction pipelines into images. The raw data and reduced images are stored on disc and transferred to the data archive centre. More details on the integration of SCUBA-2 into the JCMT observatory control system can be found in Walther et al. (2010).

4.1 Room temperature electronics and data acquisition

The MCE is a self-contained crate that performs a number of functions. It sets the detector and heater bias, the bias (and feedback values as appropriate) for the three SQUID stages, controls the multiplexing rate and reads the DC-coupled signals from a 32 × 41 sub-array. In the standard data readout mode the MCE reports a low-pass filtered feedback value for every bolometer. There is one MCE crate per sub-array and the units are physically located on the outside of the main instrument. An address card in the MCE controls the time-division multiplexing by turning on one row of first stage SQUIDs at a time (see Fig. 7). Each bolometer is revisited at a rate of 13 kHz (80 μs) during the multiplexing, which far exceeds the bolometer response time. Separate readout cards are coupled to a set of eight columns. As the current through a bolometer changes, as a result of power changes during an observation, a digital feedback servo (PID loop) is used to calculate the appropriate change to the feedback values sent to the SQ1 stage. Hence, these feedback values represent a measurement of the optical power changes and are the nominal MCE outputs. The SQ1 signals of one column are summed in a coil coupled to one second stage SQUID (Section 3.4.3). More information on the design and operation of the MCE can be found in Battistelli et al. (2008).

Each sub-array has a dedicated DA computer that sends commands to the MCE and receives data packets in return. The DA software is based on a system running RTAI Linux. Data are packaged by the MCE into frames that consist of a house-keeping block

followed by the data. The SCUBA-2 real time sequencer (SC2RTS) coordinates and controls the tasks on each of the DA computers. The SC2RTS is a VME bus crate that takes commands from the main observatory RTS for coordinating instrument data-taking with the telescope actions. The sync box ensures that all sub-arrays clock out their data frames at exactly the same time. The data frames, together with house keeping information, are packaged by the DA computers into data files that are then subsequently passed to the data reduction pipelines. With SCUBA-2 operating in scan mode these data taking sequences can last up to 40 min and contain many hundreds of thousands of frames. Since these data sets can be very large they are broken down into smaller sub-files typically written to disc every 30 s. The files are written to disc in Starlink NDF format (Jenness et al. 2009) and contain header and house-keeping information. The 180 Hz frame rate for SCUBA-2 translates to a data rate of approximately 4 MB s^{-1} (raw, uncompressed data) at each wavelength. In terms of a 12 h observing night this is equivalent to typically 100 GB of compressed data.

4.2 Data reduction pipelines

Data processing pipelines have been developed for SCUBA-2 using the established ORAC-DR pipeline infrastructure (Cavanagh et al. 2008). There are four pipelines running simultaneously at the telescope, two for each wavelength (see Fig. 10), which provide rapid feedback to observers on the quality of the data in real time. The 'quality assurance' (QA) pipeline processes data for assessing the instrument performance and produces sensitivity estimates, flat-field updates and sub-array noise performance plots. The 'summit pipeline' is designed to produce a quick-look map of the data. For the summit pipeline to run in real time it uses a curtailed version of the data reduction software described in Section 8. The pipeline can also be run in a highly flexible and configurable off-line mode ('science pipeline'), making use of science data derived from the whole night (or multiple nights), and the optimized data reduction recipes available from the Submillimetre User Reduction Facility (SMURF) map-maker (Section 8.1). The data files are transferred to the JCMT Science Archive (JSA; Gaudet et al. 2008) at the Canadian Astronomy Data Centre (CADC) in Victoria (Economou et al. 2011) within a few minutes of their appearance on disc. The primary aim of the JSA is to increase the productivity of the telescope by making science-ready data products available to the JCMT community. Hence, the data are reduced on a daily basis and fully processed images are made available to the project Principal Investigator within 24 h.

5 OBSERVING MODES

Since the major goal of SCUBA-2 is to conduct wide-field surveys of the sky the most efficient way to do this is to scan the telescope. To be able to recover large-scale structures in the presence of slowly varying baselines (caused primarily by sky emission, extinction and instrumental $1/f$ noise) the scan pattern must modulate the sky both spatially and temporally in as many different ways as possible. Spatial modulation is achieved by scanning the same region at a number of different position angles to achieve cross-linking. Temporal modulation is incorporated by visiting the same region on different time-scales. A number of scan patterns have been developed giving optimum coverage within the constraints of telescope motion (Kackley et al. 2010).

5.1 Scan modes

The telescope operates in a routine scanning mode for SCUBA-2 for which the type of scanning pattern adopted depends on the size of field to be observed. The scan pattern parameters (primarily the telescope speed and scan spacing) are chosen to ensure the effective integration times across the mapped region are as uniform as possible, as well as making it easy to define the shape of the region.

5.1.1 Small-field observations

For small fields, less than about the array footprint on the sky, constant speed 'DAISY' scans are the preferred observing pattern.[8,9] In this mode the telescope moves in a pseudo-circular pattern that keeps the target coordinate on the arrays throughout the integration. The telescope is kept moving at a constant speed to maintain the astronomical signal at a constant frequency. The pattern on the sky is defined by two parameters: R_0, the radius of the requested map, and R_T, the turning radius. The optimization of the DAISY observing mode involves identifying the parameters that provide a pattern that: (a) maximizes the on-source integration time for a given elapsed time (minimizing noise) and (b) gives uniform coverage within a 3 arcmin diameter at the centre of the image. The DAISY scan pattern in Fig. 11 (top left and top right) is optimized for the case in which R_0 and R_T are both equal to 0.25 times the array footprint.

The limitation of this mode is that the speed is constrained by the acceleration limit of the telescope (600 arcsec s^{-2} in true azimuth). When 1/cos(elevation) reaches $\sim$3 (elevation of $\sim$70°) this acceleration limit is exceeded and the pattern tends to fail. Fig. 12 (top) shows the image plane and exposure time map for the standard DAISY pattern. Although the DAISY scan is designed for small and compact sources of order 3 arcmin or less in diameter, there is significant exposure time in the map to more than double this size. The DAISY scan maximizes the exposure time in the centre of the image. For example, an image in which the output map pixel sizes have been set to 2 and 4 arcsec (at 450 and 850 μm, respectively), has an exposure time in the central 3 arcmin region of $\sim$0.25 of the total elapsed time of an observation. Fig. 12 (top right) shows how the uniformity of the noise varies as a function of radius for a DAISY scan. Given that the noise level increases by 40 per cent at a radius of 3 arcmin, this mode is useful for mapping point-like (unresolved) or compact objects of order 3–6 arcmin in diameter and less. All calibration sources (Section 6) are observed with the DAISY scanning mode.

5.1.2 Large-field observations

For fields just larger than the instrument field of view up to degree-sized scales, a map pattern called 'PONG' is used as the scan mode.[10] In this case the map area is defined to be square and the telescope tracks across the defined sky area, filling it in by 'bouncing' off the walls of this area. A further innovation is to round off the corners, making the transition at the walls curved and thereby keeping the telescope acceleration more uniform ('CURVY PONG'). Once a pattern is completed the map is rotated and the pattern is repeated at a new angle. This fulfils the criterion of cross-linking

[8] This was inspired by a similar mode used at the Green Bank Telescope.
[9] Operationally, this is often referred to as a constant velocity DAISY scan.
[10] This is based on the 'bouncing billiard ball' scan pattern developed for SHARC-II.

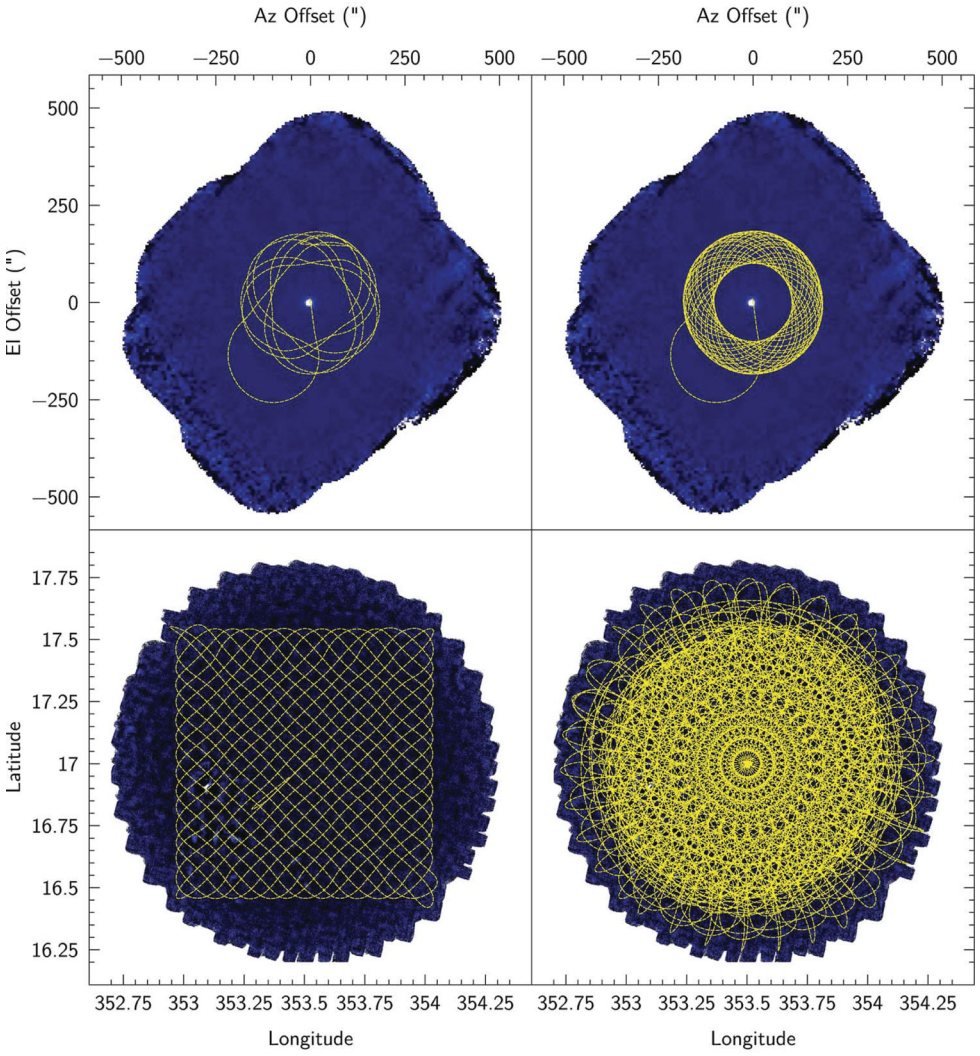

Figure 11. Telescope track in offsets of azimuth and elevation for the SCUBA-2 observing patterns. Top left: a single rotation of the DAISY pattern; top right: multiple rotations of the DAISY pattern for a typical map based on a 3 arcmin demand diameter; bottom left: a single PONG pattern; bottom right: multiple rotations of the PONG pattern for a typical map based on a 30 arcmin demand diameter. The blue background represents the total covered area of sky during an observing pattern.

scans and providing as much spatial modulation as possible. Fig. 11 (bottom left and bottom right) shows an example telescope track for a PONG map with a diameter of 30 arcmin. The parameter space of the telescope speed, the spacing between successive rows of the basic pattern and the number of rotations have been optimized to give the most uniform coverage across the requested field. Fig. 12 (bottom) shows the image plane and exposure time map for a 30 arcmin diameter PONG pattern. The PONG scan maximizes the field coverage and maintains even time uniformity. In this case output map pixel sizes of 2 and 4 arcsec (at 450 and 850 μm, respectively) give an exposure time in the central 3 arcmin region that is ∼0.014 of the elapsed time. Fig. 12 (bottom right) shows how the uniformity of the noise varies as a function of radius for a PONG scan. The noise remains uniform across the field, never increasing above 20 per cent relative to the centre of the map, out to the edge of the field.

5.2 Flat-fielding

The SCUBA-2 sub-arrays are flat-fielded using responsivity measurements derived from fast heater ramps. The bolometer signal current is determined from a series of different heater outputs consisting of a triangle wave of the order of a few pW (peak-to-peak) about a reference level. The inverse of a linear fit to the current as a function of heater power is the flat-field solution, with the responsivity ($A\,W^{-1}$) being the gradient. Bolometers are rejected that do not meet specific responsivity criteria (i.e. are deemed to be physically too low or high in value), if their response is non-linear, or if the S/N of the measurement is poor. A flat-field measurement is performed at the start and end of every observation using a 5–10 s repeating current ramp. The resulting flat-field is applied in the data reduction process for science maps (Section 8.1). The stability of the flat-field is usually excellent, with less than 1 per cent variation in the number of bolometers meeting the acceptance criteria and less than 2 per cent variation in mean responsivity on a sub-array over an entire night of observations.

5.3 Pointing and focusing

The telescope is accurately pointed and focused using images derived from short DAISY scans of a bright, compact source. For

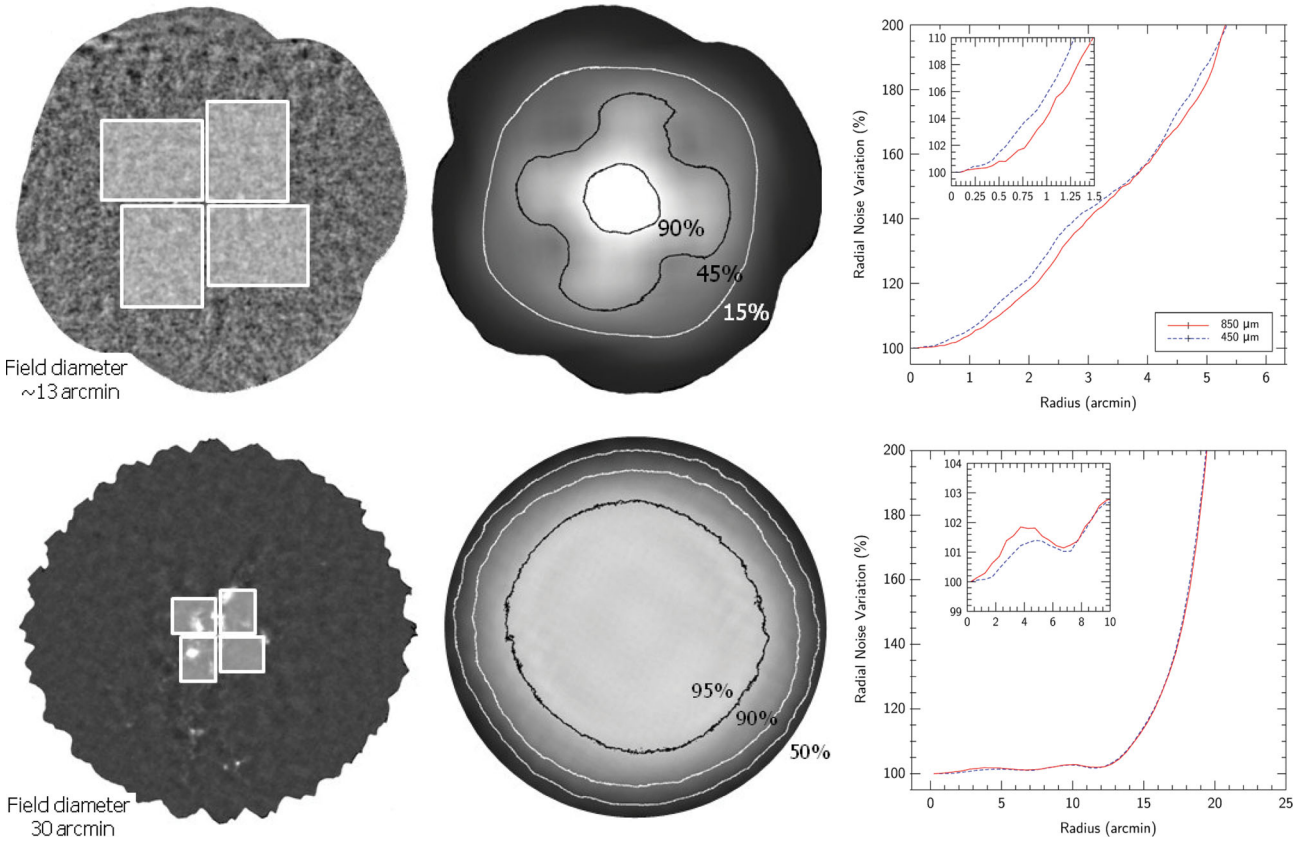

Figure 12. Left: resultant images from a typical DAISY (top) and 30 arcmin PONG (bottom) scan with the array footprint shown for scaling purposes; middle: exposure time images with contours at 90, 45 and 10 per cent of the peak value for DAISY (top) and 95, 90 and 50 per cent for PONG (bottom); right: radial noise profile in which the percentage increase in the rms noise is plotted as a function of map radius, for DAISY (top) and 30 arcmin PONG scan (bottom).

pointing, a fitted centroid to the resultant image generates offsets from the nominal position. These are then passed back to the telescope control system to make adjustments in the azimuth/elevation position. For focus, an image is taken for each of five different offsets of the secondary mirror (in three axes). A parabolic fit to the peak signal in each image generates an optimum focus offset which is passed to the secondary mirror controller.

6 CALIBRATION

The calibration of ground-based submillimetre observations can be particularly problematic because of changes in the atmospheric opacity on short time-scales (Archibald et al. 2002). The process of calibrating an observation requires two major steps. First, the attenuation of the astronomical signal by the atmosphere is determined preferably along the line of sight. Secondly, astronomical images are calibrated by reference to a flux standard. The companion paper Dempsey et al. (2013) describes the calibration of SCUBA-2 data in more detail.

6.1 Extinction correction

The transmission of the atmosphere in the submillimetre is highly wavelength dependent (as shown in Fig. 3) and depends primarily on the level of precipitable water vapour (PWV). At the JCMT weather conditions are categorized in terms of a 'weather band' with a scale from 1 to 5, with 1 being the driest and 5 the wettest. The weather band is derived from either direct measurements made at 225 GHz using a radiometer at the nearby CSO, or from a dedicated water vapour monitor (WVM) at the JCMT (Wiedner et al. 2001). The 'CSO tau' measurement is derived from a fixed azimuth sky-dip (due south) and reports the zenith opacity every 15 min. However, since the PWV can change on very short time-scales at the JCMT, it is monitored at a faster rate using a separate WVM looking directly along the line of sight of the observation. The WVM estimates the level of PWV from the broadening of the 183 GHz water line in the atmosphere at intervals of 1.2 s. Scaling the WVM measurement to a zenith opacity value shows a very close correlation to the 'CSO tau', particularly during the most stable parts of the night (9 pm until 3 am) (Dempsey et al. 2013).

Over the commissioning period the extinction relationships (at each SCUBA-2 waveband) with PWV and hence τ_{225} have been derived by analysing observations of sources of known flux density. The following relationships have been derived between the opacities at the SCUBA-2 wavebands and the 225 GHz scaled measurements from the WVM:

$$\tau_{450} = 26.0(\tau_{225} - 0.012), \quad (1)$$

$$\tau_{850} = 4.6(\tau_{225} - 0.0043). \quad (2)$$

These relationships are subsequently used in the extinction correction stage during the process of making maps (Section 8.1).

6.2 Flux calibration

Primary calibration is taken from brightness temperature models of Mars (Wright 1976) and Uranus (Moreno 2010[11]), and has been extended to include a number of compact 'secondary' sources evenly spread over the sky. These secondary calibrators can take the form of late-type stars or compact H II regions. A flux conversion factor (FCF) is derived from the DAISY observation of a standard source and converts the raw bolometer signals into janskys. The calibration of the bolometer heater (Section 3.4.2) ensures that each sub-array in a focal plane reports the same optical power when observing an astronomical source and hence only a single FCF is needed at each waveband. The FCF depends on the photometry required for a particular source morphology and values are derived that are appropriate for both estimating the peak flux (usually applicable for an unresolved, point source) or the integrated flux (for an extended source). A data base of secondary calibrators continues to be established to cover as much of the right ascension range as possible (Dempsey et al. 2013).

7 ON-SKY PERFORMANCE

7.1 Typical observing sequence

Each SCUBA-2 observation, based on either a DAISY or PONG observing pattern, follows an identical sequence. Once the telescope has been slewed to the appropriate source a fast array setup is carried out (Section 3.4.1). An observation then starts with a 10 s dark-noise measurement undertaken with the shutter closed. As the shutter opens to the sky, the power change is dynamically balanced by the heater tracking process (Section 3.4.2). Once the shutter is fully open and the power balance is stable, a flat-field measurement is carried out (Section 5.2). The heater carries out another small track at the end of the flat-field to compensate for any final sky power change. A science observation is then undertaken and typically lasts 30–40 min, although pointing, focusing and calibration observations are much shorter (typically 5 min). At the end of the observation there is another heater track before a final flat-field is carried out. Finally, the shutter closes and heater tracking restores the power balance to the dark value.

7.2 On-sky sensitivity

The sensitivity on the sky is represented by the noise equivalent flux density (NEFD) which is the flux density that produces a S/N of unity in 1 s of integration time. At the shorter submillimetre wavelengths the NEFD is particularly heavily dependent on the weather conditions. The NEFD values are calculated in a similar way to the dark NEP (see Section 3.5.2). A sky NEP value for each bolometer is calculated from the time series of the first sub-scan of an observation, and the responsivity as before from the flat-field measurement. The NEFD is then given by NEFD $= (\mathrm{NEP}_{\mathrm{sky}}\mathrm{FCF}_{\lambda})/\eta$, where the FCF is the flux conversion factor determined from a flux calibrator (Section 6.2) and η is the sky transmission. As in the case of the dark NEP a weighted average is used for the corresponding sky value. Fig. 13 shows how the NEFD varies as a function of sky transmission for both the SCUBA-2 wavebands. In terms of a direct bolometer-to-bolometer comparison, the SCUBA-2 values are 5–10 per cent better than SCUBA at 450 μm, and about the same at 850 μm. The NEFD values in 'good' observing conditions are typically 400 and 90 mJy $s^{1/2}$ at 450 and 850 μm, respectively, at least a factor of 2 worse than predicted based on a model of the instrument, telescope and Mauna Kea sky. A major contributor to these sensitivity figures is undoubtedly the higher-than-expected measured dark NEP (Section 3.5.2), although it is also possible that there are contributions from instrument and/or telescope that are not accounted for. This remains work under investigation.

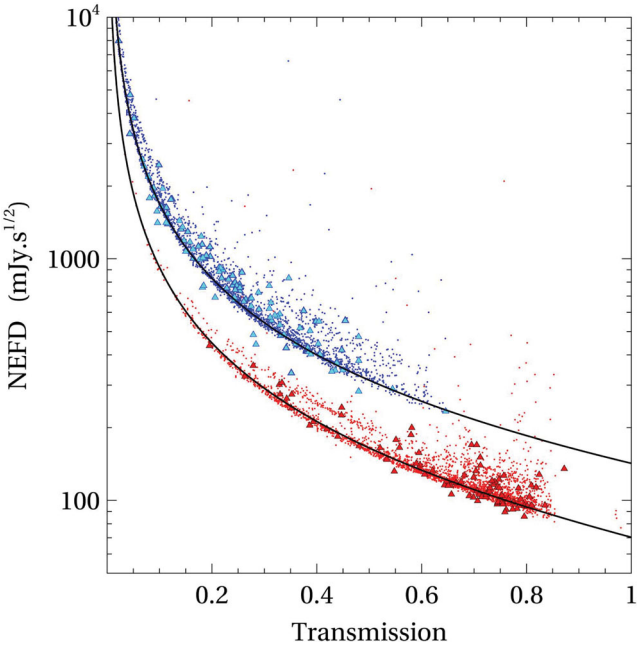

Figure 13. Measured NEFD for each SCUBA-2 waveband as a function of fractional sky transmission. The blue points are for 450 μm and the red points are for 850 μm. The triangle symbols represent NEFD estimates taken directly from calibration observations using the measured rms noise in the map and the FCF.

7.3 Sensitivity limits and mapping speed

The rms noise in a map has been shown to integrate down as expected according to time$^{-1/2}$ as shown in Fig. 14 for an ∼7 h observation. In practical terms, a DAISY field of 3 arcmin in diameter can reach a level of ∼1 mJy at 850 μm in around 3 h (in good conditions and including observing overheads), whilst for a 1° diameter field a sensitivity limit of 6 mJy can be obtained in about 7 h. Table 3 lists a selection of detection limits for the SCUBA-2 wavebands for various observing mode configurations.

Since the per-bolometer NEFDs are very similar to SCUBA, the SCUBA-2 mapping speed improvement is largely governed by the increase in detector count. Other factors include significantly lower observing overheads for the SCUBA-2 mapping modes than for the scan strategies used by SCUBA (e.g. no sky chopping). This results in mapping speed improvements of 100 and 150 times that of SCUBA for 450 and 850 μm, respectively.

7.4 Image quality

Fig. 15 shows high S/N images of the beam shapes at 450 and 850 μm, based on, respectively, a 54 and 80 image mosaic of DAISY scans of Uranus (typical disc diameter of 3 arcsec). The beams are fitted using two Gaussian components, namely a narrow

[11] Moreno R. 'Neptune and Uranus brightness temperature tabulation', ESA *Herschel* Science Centre, ftp://ftp.sciops.esa.int/pub/hsc-calibration, 2010.

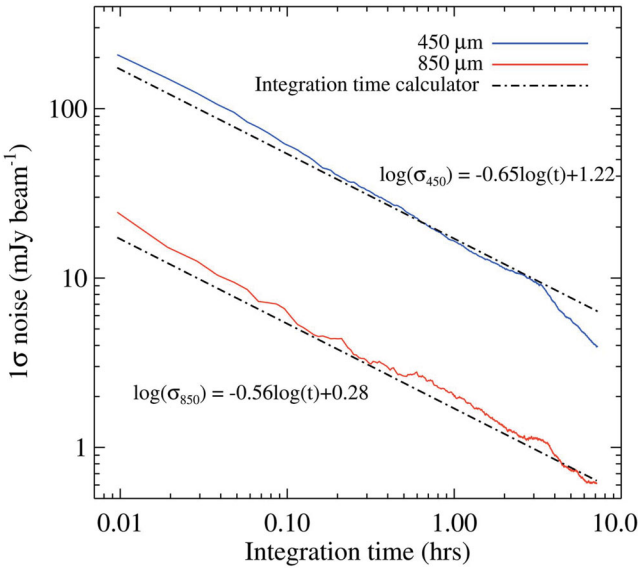

Figure 14. Measured rms noise in a 3 arcmin diameter DAISY image as a function of observing time for an ∼7 h 'blank-field' observation taken in good observing conditions ($\tau_{225} \sim 0.06$). The equations for rms noise as a function of observing time are as a result of a least-squares fit to the data (where the time, t, is in hours). The dashed lines represent the predicted rms noise from the SCUBA-2 Integration Time Calculator based on a median opacity for the set of observations (see http://www.jach.hawaii.edu/jac-bin/propscuba2itc.pl). The observation represents a co-add of 11 separate observations taken over a period of several nights. As can be seen most evidently at 450 μm the weather conditions improved significantly for some of the latter observations. Top: 450 μm (blue); bottom: 850 μm (red).

Table 3. Detection limits in mJy for the SCUBA-2 observing modes. These have been calculated based on τ_{225} values of 0.04 and 0.065 at 450 and 850 μm, respectively, and assuming a source with average airmass of 1.2. The number associated with the PONG refers to the demand diameter of the map in arcsec.

Observing mode		450 μm (mJy)	850 μm (mJy)
DAISY	(3 σ,1 h)	39	5.6
	(5 σ,10 h)	21	2.9
PONG900	(3 σ,1 h)	85	11.9
	(5 σ,10 h)	44	6.3
PONG1800	(3 σ,1 h)	166	23
	(5 σ,10 h)	87	12.2
PONG3600	(3 σ,1 h)	361	49
	(5 σ,10 h)	189	26
PONG7200	(3 σ,1 h)	732	98
	(5 σ,10 h)	384	51

main-beam and a wider secondary component. The main-beam widths (full-width at half-maximum), after de-convolving the Uranus disc, are 7.9 and 13.0 arcsec at 450 and 850 μm, respectively, whilst the secondary component has widths of 25 and 49 arcsec. It is estimated that the main-beam widths are 6 and 2 per cent higher than expected from a perfect optical system. The two-component fit reveals that the main-beam has an amplitude of 94 and 98 per cent at 450 and 850 μm, respectively, which equates to integrated power levels of 60 and 75 per cent (i.e. 40 and 25 per cent of the total power lies in the secondary component). The large ring visible in Fig. 15

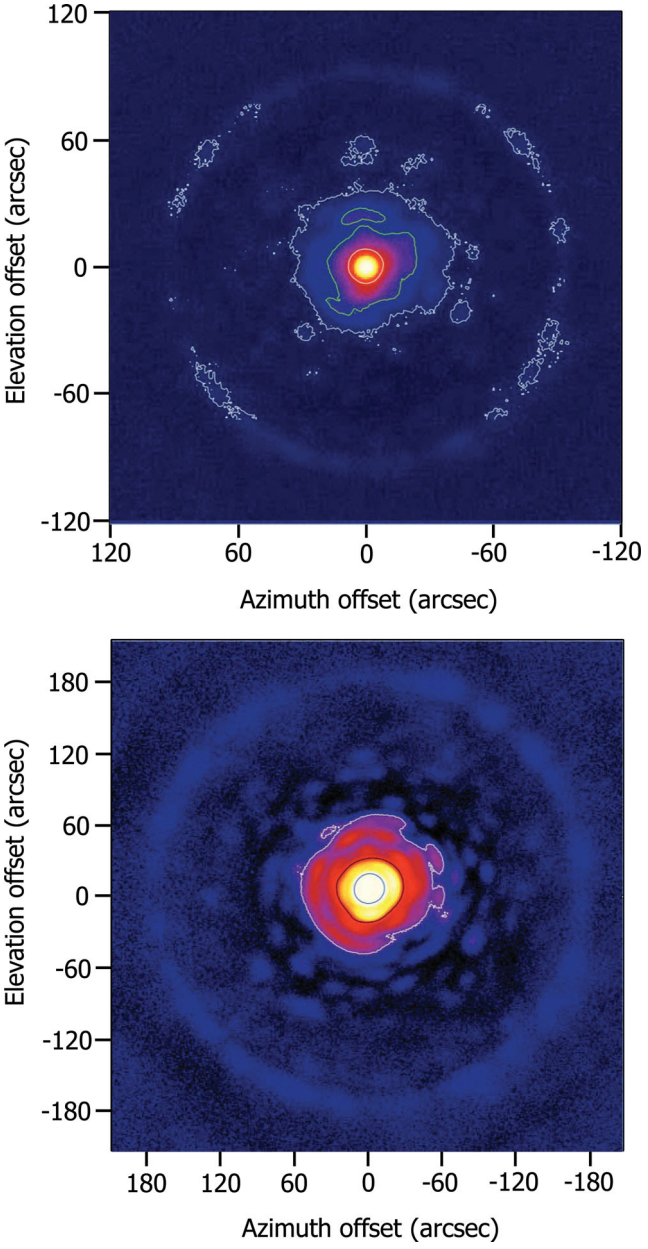

Figure 15. Measured beam using DAISY scanning of Uranus. Both plots have a log colour table to show the detail in the diffraction pattern. Top: 450 μm with contours set at 0.1 (white), 1 (green) and 10 per cent (white) of the peak amplitude. Bottom: 850 μm with contours set at 0.1 (white), 1 (black) and 10 per cent (blue).

is due to scalloping of the telescope panels since the focal length of the primary dish and panels are not exactly the same. This has an amplitude ∼0.1 per cent of the peak at 450 μm. Further details of the beam characterization can be found in Dempsey et al. (2013).

To reconstruct maps to the highest possible degree of accuracy and image quality the relative position on the sky of each bolometer in the focal plane must also be determined. This is achieved by scanning every single bolometer in each focal plane across a bright source (such as Saturn or Mars), so that a map can be created from each bolometer. Since the position of the planet and telescope are known, the relative position of the bolometers can be determined. The results also demonstrate that there is very low field-distortion (∼2 per cent) across each focal plane.

8 DATA REDUCTION AND MAP-MAKING

SCUBA-2 data are reduced and images constructed using the SMURF (see the companion paper Chapin et al. 2013), a software package written using the Starlink software environment (Jenness et al. 2009). By utilizing SMURF within the data reduction pipeline fully calibrated, publication quality images can be obtained.

8.1 Dynamic iterative map-maker

The foundation of map-making within SMURF is an iterative technique that removes most of the correlated noise sources in parallel with a simplified map estimator. To accomplish this an overall model of the observed signal is constructed, breaking down the contributing components as appropriate. For example, the signal will have a time-varying component due to atmospheric extinction, a fixed astronomical source signature and various other sources of noise. The typical map-making algorithm is shown in the flowchart in Fig. 16. The initial step in the map-maker takes the individual sub-scans and combines the data into a contiguous time series. Pre-processing applies the flat-field correction, re-samples the data at a rate that matches the requested output map pixel scale, and finally cleans the data by repairing spikes/DC steps and subtracting off a polynomial baseline from each bolometer.

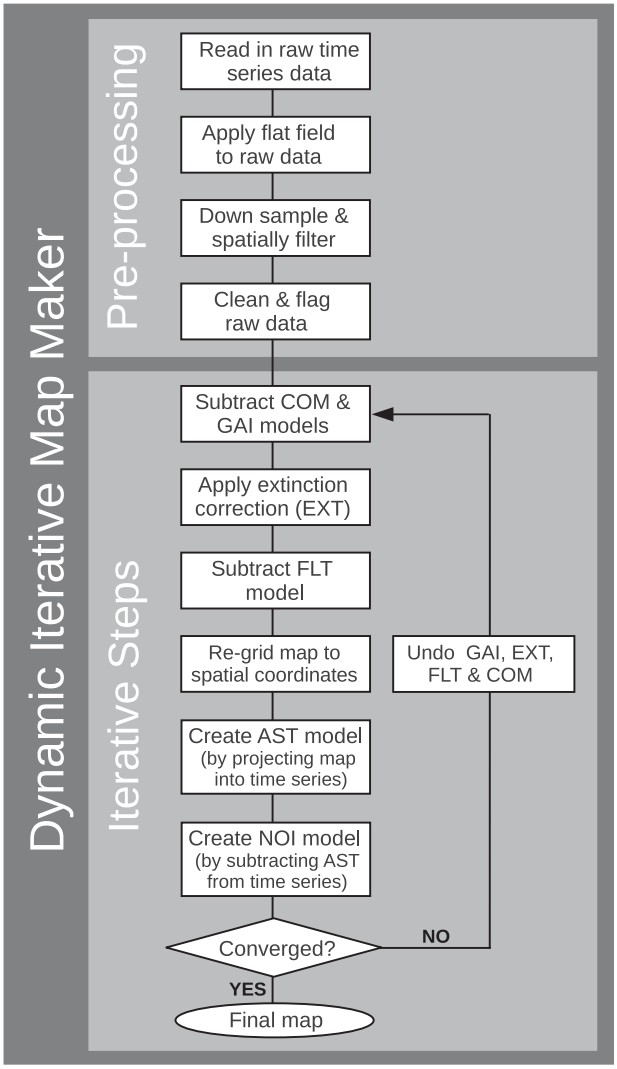

Figure 16. The SMURF map-making algorithm presented as a flowchart showing how the raw data is first pre-processed and then iteratively forms an output map through the application of a series of model components (Chapin et al. 2013).

The iterative section then commences with estimating and removing a common-mode signal (COM), usually dominated by the atmosphere, and scaling it accordingly for each bolometer (GAI) so that a common calibration can be applied later for an entire sub-array. The COM model component is the average signal from all working bolometers on a sub-array at each time-step and flags bolometers as bad if their response does not resemble that from the majority of other bolometers. A time-dependent extinction correction factor (EXT) is then applied based on measurements from the WVM (Section 6.1). The data are subsequently Fourier transformed and a high-pass filter is applied to remove residual excess low-frequency noise (FLT). The resulting cleaned and extinction-corrected data are re-gridded to produce an initial map estimate using nearest neighbour sampling. Since each map pixel will contain many bolometer samples the, noise is significantly reduced compared to the raw time series data. The map is then projected back into the time domain, thus producing the AST model containing signals that would be produced in each bolometer by the signal represented in the map. This model is then removed from the time series data giving a residual signal from which the noise for each bolometer can be determined (NOI) with an associated value of χ^2 used to monitor convergence. Since each signal component is slightly biased by signals from other components the entire process is iterated using a convergence tolerance. If the map has not changed from the previous iteration within this tolerance then the final output map is produced. If the map has changed, then the process is repeated.

The map-making process is controlled by versatile configuration files that contain all the model settings and user-definable control parameters. For example, the high-pass filter cut-off is one parameter that can be easily adjusted. The convergence tolerance can also be bypassed by setting a fixed number of iterations. However, in reality, there are a small number of standard configuration files that are customized for use with different types of observations. More details can be found in Chapin et al. (2013).

9 LEGACY SURVEYS AND EARLY SCIENTIFIC RESULTS

The key scientific driver for SCUBA-2 is the ability to carry out large-scale surveys of the submillimetre sky. Six 'legacy-style' survey programmes have been developed that are very broad based, ranging from the studies of debris discs around nearby stars to galaxy populations and evolution in the early Universe. These surveys have been approved to run from 2010 February 1 to 2014 September 30. In summary these surveys are as follows.[12]

(i) Galactic Plane Survey: more than 200 deg^2 to a 1σ depth of 15 mJy at 850 μm in 450 h.

(ii) Gould's Belt Survey: mapping of molecular clouds ($\sim$500 deg^2) to 3 mJy (850 μm) in 412 h.

(iii) Debris Disc Survey: survey of 115 nearby stars to a depth of 1.4 mJy (850 μm) in 270 h.

(iv) Local Galaxy Survey: imaging of 150 nearby galaxies down to 1.6 mJy (850 μm) in 100 h.

[12] Further information on the survey programme can be found at http://www.jach.hawaii.edu/jcmt/surveys

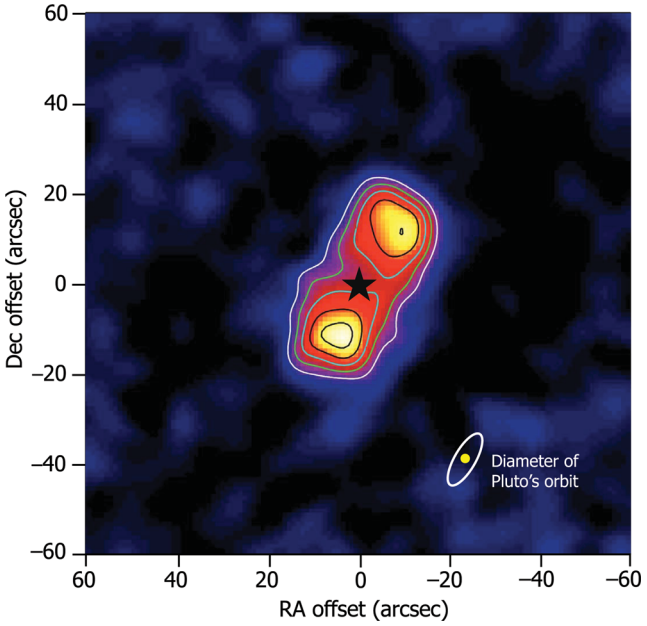

Figure 17. SCUBA-2 image of the debris disc around Fomalhaut at 850 μm. Contours start at 3σ and increase in steps of 2σ. The 'star' symbol shows the position of Fomalhaut with respect to the disc. The diameter of Pluto's orbit in our Solar system is also shown, indicating that the disc may represent a Kuiper belt like structure around the star. Image provided courtesy of the SONS Legacy Survey team.

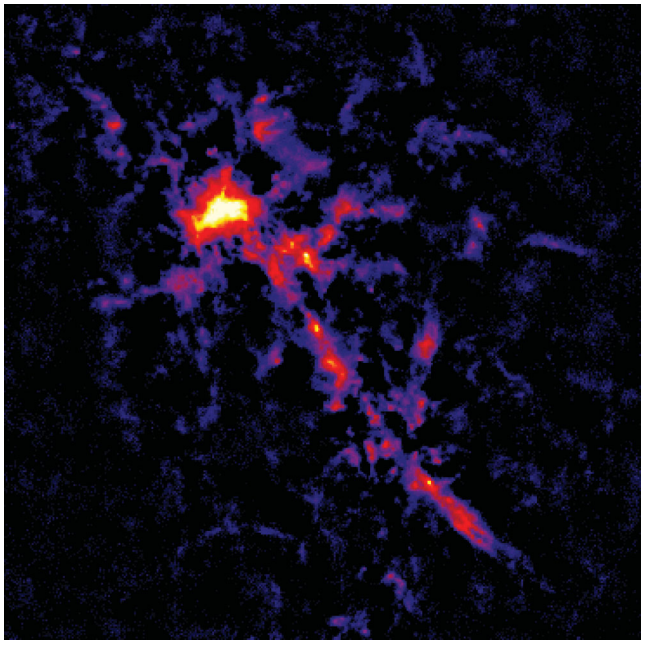

Figure 18. The high-mass star-forming region W51 in Aquila as observed by SCUBA-2 at 850 μm. The ridge of compact cores extending to the lower right in the figure runs parallel to the Galactic plane. The field size of this image is $\sim 1^\circ$ and the dynamic range is such that cores ranging in flux density from 40 Jy to <20 mJy are detected. Image provided courtesy of SCUBA-2 commissioning team.

(v) Cosmology Survey (850 μm): 10 deg^2 (several fields) to 1.2 mJy; (450 μm): 0.25 deg^2 to 1.2 mJy, for a total time of 1778 h.

(vi) SCUBA-2 ambitious sky survey: 1100 deg^2 down to 30 mJy at 850 μm in 480 h.

Although the main strength of SCUBA-2 is in wide-field mapping, the camera can also image compact sources very quickly. Fig. 17 is a short (2 h) 850 μm observation of the famous debris disc surrounding the main sequence star Fomalhaut (Holland et al. 2003) which extends to just under 1 arcmin in length. Debris discs arise from collisions amongst planetesimals in which the dusty residue spreads into a belt around the host star. Their study reveals much about the material left over after planet formation, the size of such systems compared with our own, the clearing out of comets that preceded the appearance of life on Earth, and even the detection of distant debris-perturbing planets (e.g. exo-Neptunes) that cannot be found by any other technique. The SCUBA-2 image took just one-fifth of the time of the previous SCUBA map to the same S/N level. Given that the per-bolometer NEFD values are very similar, the gain over SCUBA for compact and point-like source is largely due to not having to employ sky chopping to remove the atmosphere and 'jiggling' of the secondary mirror to produce a Nyquist-sampled image. The disc is comparable to the size of the Kuiper belt in our own Solar system and studying such discs therefore gives valuable insight into planetary system formation and evolution in our Galaxy.

Wide-field imaging of sites of star formation in our own Galaxy is one of the key elements of several of the legacy surveys. A full understanding of the star formation process also requires an appreciation of how the rare, massive stars form and shape the evolutionary history of giant molecular clouds and subsequent star and planet formation. The early stages of high-mass star formation are not well understood, largely because they occur so fast and are consequently rare. A census of high-mass star formation throughout the Galaxy is possible with SCUBA-2. Fig. 18 shows a SCUBA-2 map at 850 μm of the W51 star-forming region, containing a ridge of massive star-forming cores running parallel to the Galactic Plane. Studies such as this will show the rarest of evolutionary phases and allow an understanding of what defines the highest mass end of the stellar initial mass function. The sensitivity of SCUBA-2 equates to a mass sensitivity of 1 $\mathrm{M}_\odot$ at a distance of 3 kpc and of 180 $\mathrm{M}_\odot$ at 40 kpc, sufficient to detect all the significant high-mass and cluster forming regions throughout the Galaxy.

Another key area of the survey programme is to image the cold dust in nearby spiral galaxies. The bulk of star formation activity in nearby spirals is often missed by IR studies, since most of the dust mass resides in cold, extended, low-surface brightness discs, often far from the galactic nucleus. The studies so far have revealed that up to 90 per cent of the total dust mass can be located within galactic discs. Dust temperatures are around 10–20 K and so radiate strongly in the submillimetre region. Fig. 19 shows a *Hubble Space Telescope* (*HST*) image of the famous 'Whirlpool galaxy' M51 (and associated companion NGC 5195) overlaid with SCUBA-2 colours (blue for 450 μm; red for 850). SCUBA-2 clearly detects the nuclei of these two interacting galaxies and the fainter 850 μm emission traces the optically hidden dust lanes. Furthermore, the imaging power and spatial resolution achievable allows the study of regions of hot star formation in the outer arms of the spiral galaxy.

The final example of the versatility of SCUBA-2 is an observation of one of the most massive known cluster lenses, Abell 1689 at $z = 0.18$. Rich clusters are nature's telescopes that can be used to more efficiently study distant, star-forming galaxies. Fig. 20 is a 850 μm deep DAISY map of the Abell 1689 cluster field. The total field is approximately 13 arcmin in diameter and is known to contain over 50 lensed sources spanning a redshift range 1–6. When SCUBA observed this field it detected two sources with S/N of greater than 4

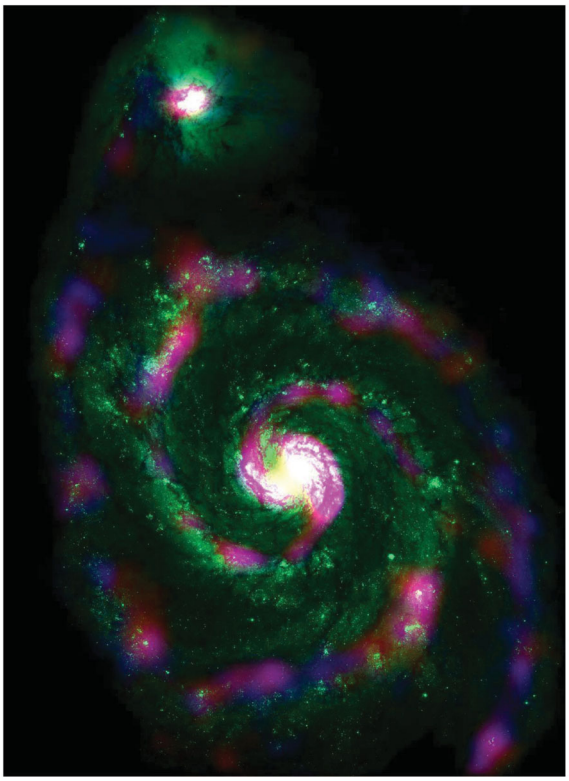

Figure 19. A composite image of the famous Whirlpool Galaxy with SCUBA-2 colours (blue for 450 μm; red for 850) superimposed on a green-scale *HST* image. The SCUBA-2 traces star formation via the emission from cold dust in the outer most regions of galaxy. The SCUBA-2 image is provided courtesy of Todd MacKenzie, and the HST image is acredited to NASA, ESA, S. Beckwith (STScI) and the Hubble Heritage Team (STScI/AURA).

and another five with tentative 3σ detections (Knudsen et al. 2008). SCUBA-2 imaged the field in a fraction of the time and detects 15 sources at greater than 5σ with many dozens at greater than 3σ, confirming a mapping speed of over 100× SCUBA. SCUBA-2 is clearly a very powerful instrument for studying the distant Universe.

10 CONCLUSIONS

SCUBA-2 is the world's largest format camera for submillimetre astronomy. It represents a major step forward in submillimetre instrumentation in terms of the detector and array architecture, observing modes and dedicated data reduction pipelines. The new technologies developed for SCUBA-2 represent a major strategic investment on behalf of the JCMT and instrument funding agencies. The instrument has already shown incredible versatility with astronomy applications being very broad based, ranging from the study of Solar system objects to probing galaxy formation in the early Universe. An imaging polarimeter (Bastien et al. 2011) and Fourier transform spectrometer (Gom & Naylor 2010) will also be available to allow the mapping of magnetic field lines and imaging medium-resolution spectroscopy, respectively.

SCUBA-2 maps large areas of sky 100–150 faster than SCUBA to the same depth, and such improved imaging power will allow the JCMT to exploit fully the periods of excellent weather on Mauna Kea. SCUBA-2 is currently undergoing a series of six unique legacy surveys for the JCMT community. These are highly complementary to the wider, but shallower, surveys undertaken by *Herschel*, and are vital to fully exploit the capabilities of the new generation submillimetre interferometers and future facilities such as ALMA, CCAT and *SPICA*.

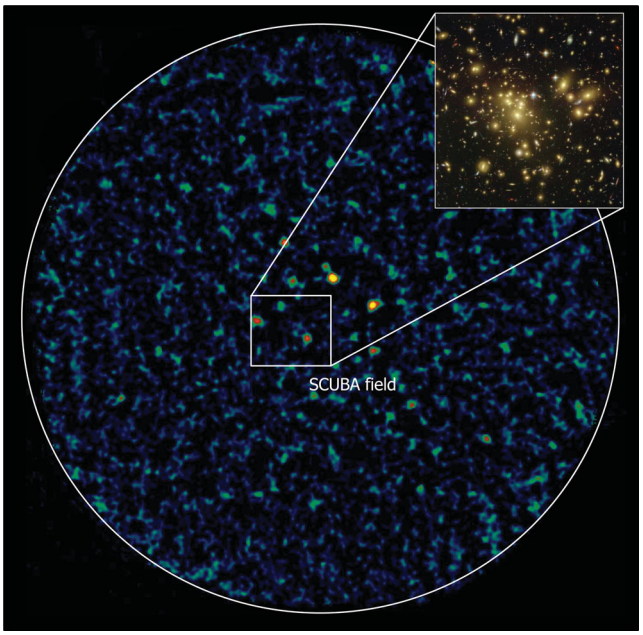

Figure 20. The massive lensing galaxy cluster Abell 1689 observed by SCUBA-2 at 850 μm. The central inset shows the approximate region observed by SCUBA and the top-right inset shows an *HST* ACS image of the field. The new SCUBA-2 map detects 15 far-IR sources seen through the massive core of this cluster. The foreground mass amplifies the fluxes of the background source, enabling fainter sources to be detected, below the blank-field confusion limit of the JCMT. Image is provided courtesy of the SCUBA-2 Guaranteed-Time team.

ACKNOWLEDGEMENTS

The JCMT is operated by the Joint Astronomy Centre on behalf of the Science and Technology Facilities Council of the United Kingdom, the Netherlands Organization for Pure Research and the National Research Council of Canada. Additional funds for the construction of SCUBA-2 were provided by the Canada Foundation for Innovation.

REFERENCES

Ade P. A. R., Pisano G., Tucker C., Weaver S., 2006, in Zmuidzinas J., Holland W. S., Withington S., Duncan W. D., eds, Proc. SPIE Conf. Ser. Vol. 6275, Millimeter and Submillimeter Detectors and Instrumentation for Astronomy III. SPIE, Bellingham, p. 62750U

André P. et al., 2010, A&A, 518, L102

Archibald E. et al., 2002, MNRAS, 336, 1

Atad-Ettedgui E. et al., 2006, in Atad-Ettedgui E., Antebi J., Lemke D., eds, Proc. SPIE Conf. Ser. Vol. 6273, Optomechanical Technologies for Astronomy. SPIE, Bellingham, p. 62732H

Audley M. D., Pisano G., Holland W. S., Duncan W. D., Parkes W., Ade P. A. R., 2004, in Zmuidzinas J., Holland W. S., Withington S., eds, Proc. SPIE Conf. Ser. Vol. 5498, Millimeter and Submillimeter Detectors for Astronomy II. SPIE, Bellingham, p. 416

Bastien P. et al., 2011, in Bastien P., Manset N., Clemens D. P., St-Louis N., eds, ASP Conf. Ser. Vol. 449, Science from Small to Large Telescopes. Astron. Soc. Pac., San Francisco, p. 68

Battistelli E. S. et al., 2008, J. Low Temp. Phys., 151, 908

Bintley D. et al., 2010, in Holland W. S., Zmuidzinas J., eds, Proc. SPIE Conf. Ser. Vol. 7741, Millimeter, Submillimeter and Far-Infrared Detectors and Instrumentation for Astronomy V. SPIE, Bellingham, p. 774106
Bintley D., Kuroda J. T., Starman E. G., Craig S. C., Holland W. S., 2012a, in Holland W. S., Zmuidzinas J., eds, Proc. SPIE Conf. Ser. Vol. 8452, Millimeter, Submillimeter and Far-Infrared Detectors and Instrumentation for Astronomy VI. SPIE, Bellingham, p. 84523C
Bintley D. et al., 2012b, in Holland W. S., Zmuidzinas J., eds, Proc. SPIE Conf. Ser. Vol. 8452, Millimeter, Submillimeter and Far-Infrared Detectors and Instrumentation for Astronomy VI. SPIE, Bellingham, p. 845208
Blain A., Smail I., Ivison R. J., Kneib J.-P., 1999, MNRAS, 302, 632
Cavanagh B., Jenness T., Economou F., Currie M. J., 2008, Astron. Nachr., 329, 295
Chapin E., Berry D. S., Gibb A. G., Jenness T., Scott D., Tilanus R. P. J., Economou F., Holland W. S., 2013, MNRAS, 430, 2545
Craig S. C. et al., 2010, in Holland W. S., Zmuidzinas J., eds, Proc. SPIE Conf. Ser. Vol. 7741, Millimeter, Submillimeter and Far-Infrared Detectors and Instrumentation for Astronomy V. SPIE, Bellingham, p. 77411K
deKorte P. A. J. et al., 2003, Rev. Sci. Instrum., 74, 3807
Dempsey J. et al., 2013, MNRAS, 430, 2534
Di Francesco J., Evans N. J., II., Caselli P., Myers P. C., Shirley Y., Aikawa Y., Tafalla M., 2007, in Reipurth B., Jewitt D., Keil K., eds, Protostars and Planets V. University of Arizona Press, Tucson, p. 17
Doriese W. B. et al., 2007, Appl. Phys. Lett., 90, 193508
Dowell C. D. et al., 2003, in Phillips T. G., Zmuidzinas J., eds, Proc. SPIE Conf. Ser. Vol. 4855, Millimeter and Submillimeter Detectors and Instrumentation for Astronomy. SPIE, Bellingham, p. 73
Economou F. et al., 2011, in Evans I. N., Accomazzi A., Mink D. J., Rots A. H., eds, ASP Conf. Ser. Vol. 442, Astronomical Data Analysis Software and Systems XVII. Astron. Soc. Pac., San Francisco, p. 203
Gao X. et al., 2008, in Duncan W. D., Holland W. S., Withington S., Zmuidzinas J., eds, Proc. SPIE Conf. Ser. Vol. 7020, Millimeter, Submillimeter and Far-Infrared Detectors and Instrumentation for Astronomy IV. SPIE, Bellingham, p. 702025
Gaudet S., Dowler P., Goliath S., Redman R., 2008, in Bunclark P. S., Lewis J. R., eds, ASP Conf. Ser. Vol. 394, Astronomical Data Analysis Software and Systems XVII. Astron. Soc. Pac., San Francisco, p. 135
Glenn J. et al., 1998, in Phillips T. G., ed., Proc. SPIE Conf. Ser. Vol. 3357, Advanced Technology MMW, Radio, and Terahertz Telescopes. SPIE, Bellingham, p. 326
Gom B., Naylor D. A., 2010, in Holland W. S., Zmuidzinas J., eds, Proc. SPIE Conf. Ser. Vol. 7741, Millimeter, Submillimeter and Far-Infrared Detectors and Instrumentation for Astronomy V. SPIE, Bellingham, p. 77412E
Gostick D., Montgomery D., McGregor H., Woodcraft A., Gannaway F., 2004, in Moorwood A. F. M., Iye M., eds, Proc. SPIE Conf. Ser. Vol. 5492, Ground-based Instrumentation for Astronomy. SPIE, Bellingham, p. 1743
Holland W. S. et al., 1998, Nat, 392, 788
Holland W. S. et al., 1999, MNRAS, 303, 659
Holland W. S. et al., 2003, ApJ, 582, 1141
Hollister M. I., 2009, PhD thesis, Univ. Edinburgh
Hollister M. I., McGregor H., Woodcraft A., Bintley D., MacIntosh M. J., Holland W. S., 2008, in Duncan W. D., Holland W. S., Withington S., Zmuidzinas J., eds, Proc. SPIE Conf. Ser. Vol. 7020, Millimeter, Submillimeter and Far-Infrared Detectors and Instrumentation for Astronomy IV. SPIE, Bellingham, p. 702023
Hollister M. I., Woodcraft A., Holland W. S., Bintley D., 2008, in Duncan W. D., Holland W. S., Withington S., Zmuidzinas J., eds, Proc. SPIE Conf. Ser. Vol. 7020, Millimeter, Submillimeter and Far-Infrared Detectors and Instrumentation for Astronomy IV. SPIE, Bellingham, p. 70200Y
Hughes D. H. et al., 1998, Nat, 394, 241
Irwin K. D., 1995, Appl. Phys. Lett., 66, 1998
Irwin K. D., Hilton G. C., 2005, in Enss Chr., ed., Topics in Applied Physics, Vol. 99, Cryogenic Particle Detection. Springer-Verlag, Berlin, p. 63
Jenness T., Berry D. S., Cavanagh B., Currie M. J., Draper P. W., Economou F., 2009, in Bohlender D. A., Durand D., Dowler P., eds, ASP Conf. Ser. Vol. 411, Astronomical Data Analysis and Systems XVIII. Astron. Soc. Pac., San Francisco, p. 418
Kackley R. D., Scott D., Chapin E., Friberg P., 2010, in Radziwill N. M., Bridger A., eds, Proc. SPIE Conf. Ser. Vol. 7740, Software and Cyberinfrastructure for Astronomy. SPIE, Bellingham, p. 77401Z
Knudsen K. K. et al., 2008, MNRAS, 384, 1611
Kreysa E. et al., 1998, in Phillips T. G., ed., Proc. SPIE Conf. Ser. Vol. 3357, Advanced Technology MMW, Radio, and Terahertz Telescopes. SPIE, Bellingham, p. 319
Mather J., 1982, Appl. Opt., 21, 1125
Motte F., Andre P., Neri R., 1998, A&A, 336, 150
Murphy E. J., Chary R.-R., Dickinson M., Pope A., Frayer D. T., Lin L., 2011, ApJ, 732, 126
Siringo G. et al., 2009, A&A, 497, 945
Smail I., Ivison R. J., Blain A., 1997, ApJ, 490, L5
Tucker C., Ade P. A. R., 2006, in Zmuidzinas J., Holland W. S., Withington S., Duncan W. D., eds, Proc. SPIE Conf. Ser. Vol. 6275, Millimeter and Submillimeter Detectors and Instrumentation for Astronomy III. SPIE, Bellingham, p. 62750
Walther C. A., Gao X., Kelly B. D., Kackley R. D., Jenness T., 2010, in Radziwill N. M., Bridger A., eds, Proc. SPIE Conf. Ser. Vol. 7740, Software and Cyberinfrastructure for Astronomy. SPIE, Bellingham, p. 77400Y
Walton A. J. et al., 2005, Proc. Inst. Mech. Eng. N, J. Nanoeng. Nanosyst., 219, 11
Wang N. et al., 1996, Appl. Opt., 34, 6629
Ward-Thompson D., André P., Crutcher R., Johnstone D., Onishi T., Wilson C., 2007, in Reipurth B., Jewitt D., Keil K., eds, Protostars and Planets V, University of Arizona Press, Tucson, p. 17
Wiedner M., Hills R. E., Carlstrom J. E., Lay O. P., 2001, ApJ, 533, 1036
Woodcraft A. L., Hollister M. I., Bintley D., Gannaway F., Gostick D., Holland W. S., 2009, Cryogenics, 49, 504
Wright E. L., 1976, ApJ, 681, 415
Wyatt M. C., 2008, ARA&A, 46, 339

This paper has been typeset from a TEX/LATEX file prepared by the author.